Physics – Uspekhi **63** (1) 2 – 32 (2020)

REVIEWS OF TOPICAL PROBLEMS

PACS numbers: **07.85.–m,** 42.55.Vc, 61.05.C–

X-ray diffraction methods for structural diagnostics of materials: progress and achievements

G V Fetisov

DOI: https://doi.org/10.3367/UFNe.2018.10.038435

Contents

Abstract. **The development of X-ray diffractometry at the turn of the 21st century is presented. The review covers instrumentation development for structural studies based on the use of both standard continuously radiating X-ray generators and state-of-the-art sources of ultrashort and ultra-bright X-ray pulses. The latter technique enables investigation of the structural dynamics of condensed matter in a 4D space–time continuum with a resolution reaching a tenth of a femtosecond. New engineering approaches to enhancing the sensitivity, accuracy, and efficiency of X-ray diffraction experiments are discussed, including new and promising X-rays sources, reflective collimating and focusing X-ray optical devices, and fast low-noise and radiation-resistant position-sensitive X-ray detectors, as well as a new generation of X-ray diffractometers developed based on these elements. The presentation is focused on modern engineering solutions that enable academic and applied-research laboratories to perform X-ray diffraction studies on-site, which earlier were only feasible using synchrotron radiation sources at international resource sharing centers.**

Keywords: X-ray diffraction, synchrotron radiation, X-ray diffractometers, pulse X-ray sources, laser-plasma X-ray sources, alternative X-ray sources, X-ray free-electron lasers, reflective X-ray optics, multilayer thin-film X-ray reflectors, semiconductor position-sensitive X-ray detectors, two-dimensional hybrid pixel detectors

1. Introduction

Technological progress in the second half of the 20th century resulted in the creation of a variety of materials and substances with specific functional properties, which, while having the same chemical composition, exhibit a strong dependence on the atomic–molecular structure. These materials are of interest because their properties can be controlled by changing the structure and morphology of particles. However, in order to manage these features, operational information about the atomic–molecular structure, size, and shape of particles in each specific sample or in a batch of materials is required; hence the need for effective and accurate methods to control the structure of materials.

One of the main tools for research and diagnostics of the atomic structure, phase composition, particle morphology, and a number of other structural features of various materials is X-ray diffraction (XRD) methods [1–5]. After the discovery of the effects of X-ray diffraction and interference [6–10], methods developed on the basis of these phenomena have been successfully used for more than a hundred years to determine the structure of crystalline, conventionally crystalline, and amorphous materials, as well as to determine the size and shape of microscopic and submicroscopic particles contained in both solid and liquid states.

The principles, theory, and practice of the application of these methods are well developed and presented in the

G V Fetisov Lomonosov Moscow State University,
Department of Chemistry,
Leninskie gory 1, str. 3, 119991 Moscow, Russian Federation
E-mail: g.fetisov@mail.ru

Received 10 August 2018, revised 15 September 2018
Uspekhi Fizicheskikh Nauk **190** (1) 2 – 36 (2020)
Translated by M Zh Shmatikov; edited by A M Semikhatov

specialized and scientific literature, for example, in well-known textbooks [1–3, 5, 11–18]. Measurements that use these methods do not typically require special preparation of samples and are carried out under ordinary conditions in the open air, which compares them favorably with many other methods of control and structural diagnostics applied in the field of modern high-tech materials and nanostructures [5, 19, 20].

Throughout the hundred years of their existence, XRD methods of structural analysis have been constantly improving. Theoretical and methodological progress in this development usually went ahead of the capabilities of laboratory technology. There was even a short period when, due to the insufficient level of development of the technological capabilities of laboratory X-ray diffractometry, it was not possible to practically use a significant part of the long-developed analysis methods designed, for example, for highly disordered and noncrystalline materials, which hindered the structural analysis of macromolecular crystals. The main impediment was the low brightness of X-ray generators and the low efficiency of devices and systems used for radiation detection. However, the technological prerequisites to overcome these difficulties were created during the last two decades of the 20th century.

X-ray structure analysis (XRSA) and other methods of XRD studies were boosted in the 21st century to a qualitatively new level as a result of the radical modernization of analytical equipment. At the turn of the millennium, conceptually new X-ray sources with unprecedented high brightness appeared (synchrotron radiation sources based on resonant cyclic accelerators, microfocus X-ray tubes (XRTs) with solid and liquid anodes equipped with efficient X-ray reflectors). The production of reflective X-ray optical devices with high transmission capacity for cleaning, monochromatizing, focusing, and collimating X-ray beams was deployed [21–27]. Manufacturing commenced of new X-ray detectors [28–31], both linear (1D) and two-dimensional (2D) position-sensitive devices, which also feature high quantum sensitivity and efficiency, high amplitude energy resolution, radiation resistance, and at the same time a low level of intrinsic noise.

As a result, modern laboratory X-ray diffractometers of the latest generation have greatly outperformed the instruments manufactured even in the last decade of the 20th century in analytical capabilities: the accuracy and validity of measurements, sensitivity, and efficiency (and sometimes, their superiority) are indeed immense. This advancement made it possible to implement methods of XRD analysis that previously were mainly of academic interest because there were no technological means for their practical realization. However, the process of upgrading and improving the techniques for XRD studies not only continued without slowing down but, on the contrary, began to accelerate and expand the scope of X-ray research methods owing to the creation of new X-ray sources with unique properties and highly efficient experimental data collection systems.

In this review, we consider the dramatic expansion of the possibilities of XRD methods and technological tools of structural diagnostics of materials over the past two decades. Attention is focused on the technological developments that have recently occurred in XRD methods, such as X-rays with the highest brightness and unique time and spectral characteristics, reflective X-ray optical devices, and the latest semiconductor systems for 1D and 2D detection of X-rays. Along with the unique resource-sharing centers operating immense synchrotron radiation sources and X-ray lasers, which are briefly reviewed here, attention is focused on analytical facilities for laboratory use that are needed for the prompt solution to current problems in university and industrial laboratories.

This review only covers XRD methods that use monochromatic radiation, because they are more common than analytical methods based on a continuous emission spectrum. X-ray diffraction research methods based on continuous radiation, such as the Laue method, which is rather actively used in XRD analysis of macromolecular single crystals [32–36], or energy dispersive diffractometry of powders [34–40], are specific methods that have a rather limited practical application; their principles and current status can be found, for example, in the sources cited above.

2. Principle of X-ray structure analysis methods and their features

The XRSA techniques are related to the methods of optical measurements [41] and share the experimental design with them. Electromagnetic radiation is directed in these settings to a sample of the test substance (in this example, a single crystal) and interacts with it, while the detector of electromagnetic radiation records the result of this interaction in the form of a spatial distribution of scattering intensity, if the measurements are carried out using monochromatic radiation (Fig. 1).

If polycrystalline samples (for example, a powder consisting of small randomly oriented crystals) are explored with the same setup, the obtained intensity distribution of the radiation scattered by the sample has Debye interference rings [3, 17], qualitatively similar to an XRD pattern (Fig. 2a); its one-dimensional projection (summed over the Debye rings) is shown in Fig. 2b.

Structure determination, i.e., reconstruction of the atomic–molecular structure using XRD data, is a rather difficult task, but the methods for solving this problem are well developed, although they vary depending on specific objects and measurement methods, as follows from the monographs and textbooks that consider the basis and features of this analysis [3, 11, 16–18, 42–48].

To determine the structure of a test sample using a set of measured diffraction data [46, 49, 50], an XRD experiment model is typically used where the effects of the interaction of the probe radiation with the sample, instrumentation effects, and physical radiation parameters are taken into account. A theoretical analysis based on the comparison of a mathematical model with experimental data allows computing the structural characteristics of the sample.

The diffraction data sets obtained in the experiment, the intensities I_{m} recorded for a diffraction angle 2θ (or the corresponding diffraction vector $\mathbf{Q}$, whose absolute value is $|\mathbf{Q}| = 4\pi(\sin\theta)/\lambda$, where λ is the X-ray wavelength), and the orientation of the sample relative to the direction of the probe beam, are a diffraction image of the object under study and depend on its shape, atomic and molecular structure, and state of aggregation. For example, diffraction measurements of a single crystal yield a three-dimensional set of individual reflections observed at various orientations of the crystal relative to the primary beam direction. A combined two-dimensional projection of such a set onto a two-coordinate detector is similar to the image shown in Fig. 1.

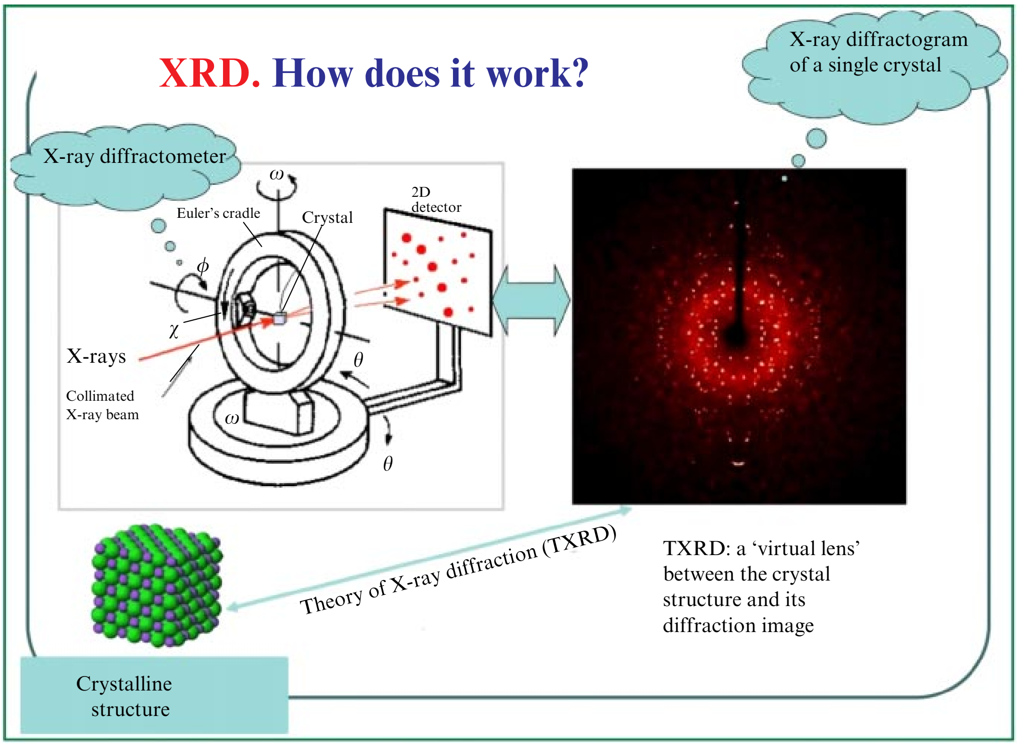

Figure 1. Block diagram of the XRSA method applied as an example to a single crystal (single crystal sample, monochromatic X-rays, angle dispersion). X-ray diffractometer setup: 2θ is the angle of X-rays scattering relative to the primary ray (X-rays); the symbols ϕ, χ, ω denote the Euler angles of rotation of a single-crystal sample. The dark inset shows the projection of a three-dimensional set of diffraction data (Bragg interference reflections and the background of scattered X-ray radiation) onto a flat two-dimensional detector in an actual experiment.

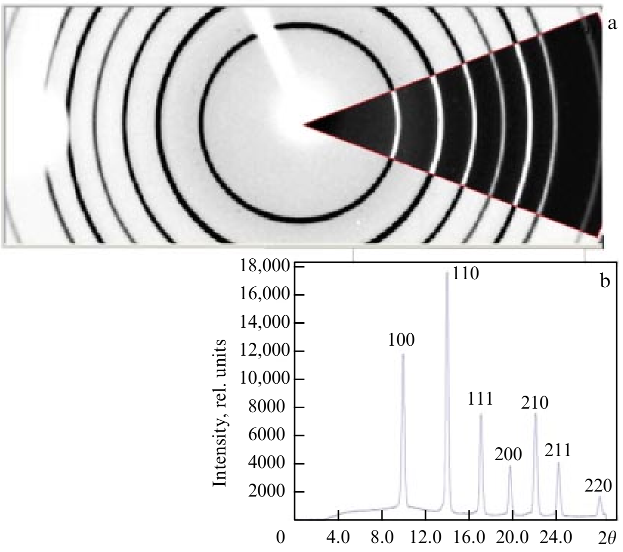

Figure 2. (a) XRD pattern in the Cu Kα radiation from an LaB$_6$ crystalline powder recorded by a two-dimensional detector; (b) one-dimensional projection of the right-hand side of the diffractogram (a) obtained by summing the intensity over Debye rings within the shaded sector.

As follows from the theory of XRSA [11, 12, 16, 51], the diffraction image of an object under study is an image of the atomic and molecular structure of the material and the shape of the sample, the observed image being associated with a prototype invisible to the human eye (atomic structure of the material) by the Fourier transformation. This transformation can and does serve as a kind of a projection 'lens', as shown schematically in Fig. 1, which enables one to 'see' the structure of the sample under study using the inverse Fourier transformation, or rather, to obtain values of its parameters — types and relative positions of atoms — as a result of XRSA. Consequently, the direct Fourier transformation allows calculating the X-ray diffractogram of the material under study using known structural parameters of the material, an option that has been widely used recently to replenish data banks for structural analysis [52] with theoretical diffractograms.

If polycrystalline samples (for example, a powder consisting of small randomly oriented single crystals) are measured in the same setup, the intensity distribution of the radiation scattered by the sample is obtained with Debye interference rings (Fig. 2a); its digitized one-dimensional projection is shown in Fig. 2b.

XRD patterns from liquids or samples of amorphous materials do not usually exhibit Bragg peaks because these substances do not have long-range order, i.e., a crystalline structure; the patterns look like the diffuse distributions that are shown for several samples in Fig. 3.

Although there is no pronounced Bragg interference, these diffraction patterns, nevertheless, also contain information about the atomic and molecular structure of the medium that generated the patterns. Analysis of scattering intensities as a function of the angle 2θ using special XRSA techniques [3, 4, 18] allows determining (reconstructing) the atomic structure of both crystalline and noncrystalline materials.

2.1 Measurement statistics in X-ray analysis

To determine a crystal structure based on XRD data using the Fourier transformation, which is the procedure employed in

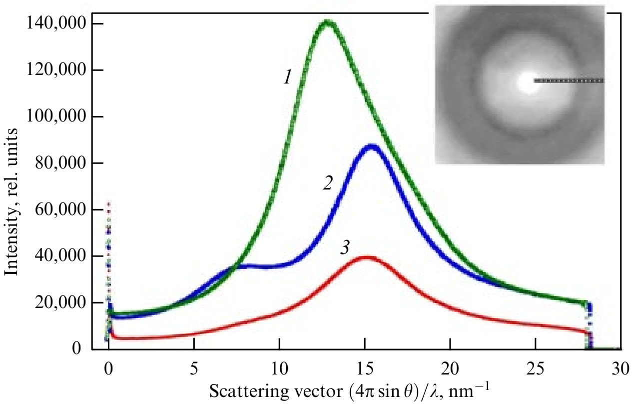

Figure 3. Examples of XRD patterns of liquid samples. Cu Kα radiation, measurements in the range of scattering angles $0° < 2\theta < 40°$ $(0 < Q < 28\ \text{nm}^{-1})$. One-dimensional cross sections of two-dimensional diffraction patterns from quartz capillaries with samples of liquids: *1* — toluene, *2* — ethyl alcohol mixed with water, *3* — suspension of Si nanocrystals in ethyl alcohol. The inset shows an example of a two-dimensional diffraction pattern of amorphous sucrose.

all XRSA methods [3, 16–18, 53], it is necessary to have the most complete set of experimentally measured intensities of coherent X-ray scattering by the substance and the angular coordinates of this scattering. In the general case, this is the distribution $I_{\text{coh}}(\mathbf{Q})$, where $\mathbf{Q}$ is the diffraction vector, also referred to as the X-ray scattering vector. To obtain reliable results of structural analysis with good resolution, the scattering intensity should be measured with a relative error of no more than 1%.

The experimental value of the scattering intensity I_{m} per unit volume of the sample is a sum of the intensity of the useful signal I_{coh} of elastic coherent scattering of X-ray photons from the distribution of the electron density of the sample and the intensity I_{bg} of the incoherent background:

$$I_{\text{m}} = I_{\text{coh}} + I_{\text{bg}} = I_0 S_{\text{F}} A + I_{\text{bg}} \,. \tag{1}$$

The intensity of the coherent scattering I_{coh} is here proportional to the intensity I_0 of the beam of primary rays incident on the object and interacting with it, but is mainly determined by the scattering capacity of the object measured by the coefficient S_{F}, usually referred to as the structural factor, that depends on the structure and morphology of the analyzed sample. The goal of XRD analysis and most XRD experiments is to measure the spatial distribution of S_{F}, i.e., to determine the intensity I_{coh} that contains this coefficient in the most accurate way. The factor A in Eqn (1) takes nondiffraction loss of intensity in the sample into account (for example, absorption and thermal vibrations of atoms). The term I_{bg} in Eqn (1) is related to incoherent contributions to the measured intensity from backgrounds of various natures, both diffraction and nondiffraction, including the electronic noise from the measuring equipment. Because discrete processes of generation and detection of X-ray photons are statistical processes described by the Poisson distribution [16, 54–56], the relative error δI_{coh} is determined in [57] by the formula

$$\delta I_{\text{coh}} = \frac{100\% \sqrt{I_{\text{m}} + I_{\text{bg}}}}{I_{\text{m}} - I_{\text{bg}}} \,. \tag{2}$$

If the count rate R is constant, i.e., if the photon flux is constant and the detector operates in a stable manner, the intensity over time t is $I = Rt$, and Eqn (2) can be written as

$$\delta I_{\text{coh}} = \frac{100\,\% \sqrt{R_{\text{m}} + R_{\text{bg}}}}{(R_{\text{m}} - R_{\text{bg}})\sqrt{t}} \,, \tag{3}$$

where R_{m} is the counting rate observed in the experiment.

Equation (3) shows that the relative error in measuring the intensity decreases as the exposure t increases; however, the duration of the experiment grows much faster than the accuracy increases and may become unacceptable. But because, according to Eqn (1), $I_{\text{coh}} \sim I_0$, which is also true for the counting rate R_{m}, the relative error δI_{coh} can be greatly reduced without unnecessary extension of the duration of the experiment. It is possible, for example, to increase the counting rate by increasing the brightness of the primary beam several-fold or by several orders of magnitude, an advancement that is technologically feasible.

Therefore, to achieve high sensitivity and accuracy of diffraction methods of the structural diagnostics of materials and substances, first of all, strong fluxes of monoenergetic photons in a high-brightness primary beam are required. It is also necessary to perform intensity measurements with maximum efficiency and minimal background and hence with minimal detector noise. In this review, we discuss technological tools and capabilities that are either already available or currently under development and which are needed to meet these requirements and to expand the scope of XRD methods for structural diagnostics of materials and substances.

3. X-ray sources

In angular-dispersion X-ray diffractometry for structural studies, monochromatic or quasimonochromatic (with a relative spectral width of $\delta\lambda/\lambda \leqslant 0.001$) electromagnetic radiation with a wavelength λ in the range $0.1-2.5$ Å (photons with energies in the range 5–124 keV) is typically used as a probe. X-rays with a wavelength $\lambda < 0.1$ Å are infrequently used in XRD studies because beams of sufficient intensity with such energies are expensive to obtain and difficult to handle, while radiation with wavelengths $\lambda > 2.5$ Å is strongly absorbed in air and in the studied materials; it is for this reason that they are not a popular tool for explorations.

X-ray was initially a term used for electromagnetic radiation generated by a beam of accelerated electrons, which are decelerated in the metal anode of an electric vacuum high-voltage diode referred to as an X-ray tube [11, 58–60]. Electromagnetic radiation with the same wavelength obtained by other methods [60–63] was called differently: gamma rays if they emerged as a result of the decay of radioactive materials, or cyclotron, synchrotron, or undulator radiation if it was generated by accelerated charged particles (most often, electrons) whose trajectories are curved by the magnetic field. Recently, with the advent of high-power pulsed optical lasers, plasma generators of X-ray radiation have become increasingly widespread [64, 65]. However, all these types of electromagnetic radiation that have different names but the same wavelength in the X-ray range are equally suitable for X-ray studies. The final result is important for the user: electromagnetic radiation with the required wavelength and sufficient intensity, regardless of how it is generated. Therefore, in this review, we refer to any electromagnetic waves with a length λ in the range $0.1-2.5$ Å as X-rays if there is no need to emphasize their relation to a specific method of generation.

The main value for users is in most cases the spectral flux density of X-ray photons with the required wavelength [photon s^{-1} mm^{-2}] ($\Delta\lambda/\lambda = 0.1\%$) incident on the analyzed object, which determines the sensitivity, resolution, and speed of analytical methods that use X-rays as a probe. If focusing optical devices are not used in an X-ray diffractometer or spectrometer, the photon flux density in the primary beam is directly related to the luminosity or spectral brilliance of the radiation source [photon s^{-1} $mrad^{-2}$ mm^{-2}] ($\Delta\lambda/\lambda = 0.1\%$), i.e., the number of quasimonochromatic photons emitted per unit time from a unit surface area of the source into a unit solid angle. An interpretation of the definitions and meaning of the characteristics of the intensity and power of radiation sources used here can be found, e.g., in [66], in Section 2.3.2 of book [34–36], in [67], or in Chapters 1 and 2 of monograph [68].

Radiation of two types of sources is currently used most often for XRD methods of structural analysis: (1) XRTs [17, 60, 69], which for more than 100 years have been the main sources of X-rays for a variety of purposes, including XRD research methods, and are most accessible to users, and (2) synchrotron radiation (SR) [34–36, 60, 61, 68, 70, 71] generated in large accelerators of electrons or positrons with an energy of several GeV. SR sources based on cyclic accelerators (synchrotrons or storage rings) have been used as X-ray generators for about 50 years, and their popularity for scientific research is constantly growing, despite the high cost of building and operating the corresponding electrophysical generating equipment.

3.1 Features of mechanisms of radiation by various sources

In XRTs and SR, X-rays are generated in very different ways [17, 34–36, 60, 61, 72], and this circumstance significantly affects the differences between their characteristics relevant for their use, primarily the spectral and polarization properties of radiation, as well as brightness.

X-rays can mainly be divided into the following groups and subgroups according to their generation mechanisms:

(1) bremsstrahlung of electrons or positrons moving with acceleration (or deceleration):

(a) nonrelativistic,

(b) relativistic;

(2) fluorescent (characteristic) radiation of stationary atoms or ions:

(a) excited by elementary particles that bombard atoms or ions;

(b) excited by photons absorbed by atoms;

(3) gamma radiation emerging as a result of radioactive decay of atomic nuclei.

Relativistic particles are those particles whose velocity v is comparable to the speed of light c, and the energy E of a particle exceeds the rest energy by a factor of more than two, i.e., $\beta = v/c \to 1$, and the energy is $E \geqslant 2m_0c^2$, where m_0 is the rest mass of the particle. The rest energy of the electron is $E_{0e} = m_{0e}c^2 = 0.511$ MeV; therefore, according to the specified criterion, electrons with an energy $E_e > 1$ MeV are regarded as relativistic particles. Electrons with an energy $E_e \gg 1$ MeV (greater by 1000 times or more) are referred to as *ultrarelativistic* particles.

To excite radiation in an XRT, electrons with an energy $E_e \leqslant 100$ keV are used, which are considered slow nonrelativistic particles. Unlike XRT radiation, SR is the electromagnetic radiation that spans a wide range of electromagnetic wave energies, including the X-ray range of the spectrum; it is emitted by electrons accelerated to ultrarelativistic velocities (usually to energies above 1 GeV) and decelerated by a magnetic field, and is described by the laws of relativistic electrodynamics. Due to the enormous difference in the speeds of the emitting electrons and the various generation mechanisms in XRTs and in synchrotrons, the spatial distribution of the radiation power is very different for these sources (Figs 4a – d) [72], and the power consumption of the generators themselves is very different (watts or kilowatts in the case of XRTs and megawatts in the case of X-ray range SR sources).

X-rays from XRTs are the sum of the radiation emitted by two types of emitters that operate based on completely different mechanisms: (1) as the bremsstrahlung of moving charges emitted by accelerated electrons from the cathode that are slowed down in the potential fields of atoms of the XRT anode material; and (2) as the characteristic fluorescence X-ray radiation of the stationary ionized intrinsic atoms of the XRT anode. Fluorescence (characteristic) X-ray radiation of stationary atoms is emitted with the same intensity in all directions, similarly to gamma radiation emitted in the decay of radioactive elements. For each electron, the bremsstrahlung of slow (nonrelativistic) electrons in an XRT is similar to cyclotron radiation [61, 68]. Due to the chaotic orientation of the trajectories of decelerating electrons in the XRT anode, this bremsstrahlung is also spherically isotropic on average, as can be seen in Figs 4a, c, f.

Nonrelativistic electrons moving along a curved path in a cyclotron [61, 68] emit electromagnetic waves in such a way that the spatial intensity distribution is described for each of them by a toroid function (Figs 4a, c) whose axis coincides with the direction of acceleration. The angles θ' and ϕ' measure the position of the current wave vector of electromagnetic radiation relative to the acceleration and linear velocity of the emitting electron. The radiation intensity relative to this direction is described by the dependence $I_v \propto \sin^2\theta'$, and the radiation intensity forward and backward with respect to the velocity vector is the same. The same conclusion holds for the bremsstrahlung radiation in an XRT during the scattering of bombarding electrons by the atomic potentials of the anode material. The motion paths of electrons are curved by the attraction of nuclei and repulsion of the electron shells of atoms (Fig. 4f). The directions and curvature radii of the trajectories of a bunch of electrons are in this case randomly distributed and therefore the axes of the corresponding intensity distribution toroids (Fig. 4a) can be oriented in any direction. Thus, the averaged distribution of the XRT radiation intensity can be approximately represented by a sphere, and the bremsstrahlung intensity can be considered to be distributed in a spherically isotropic way around the anode focus region where the deceleration and absorption of bombarding electrons occurs.

In a synchrotron, unlike an XRT, emission from relativistic electrons occurs without any contact with a condensed medium, and their radiation experiences relativistic contraction, which results in the 'headlight effect' [61], that is, rays are emitted as a narrow, almost parallel, beam directed along the path of the moving electrons (Fig. 4b). To describe the radiation of relativistic electrons that move along curved

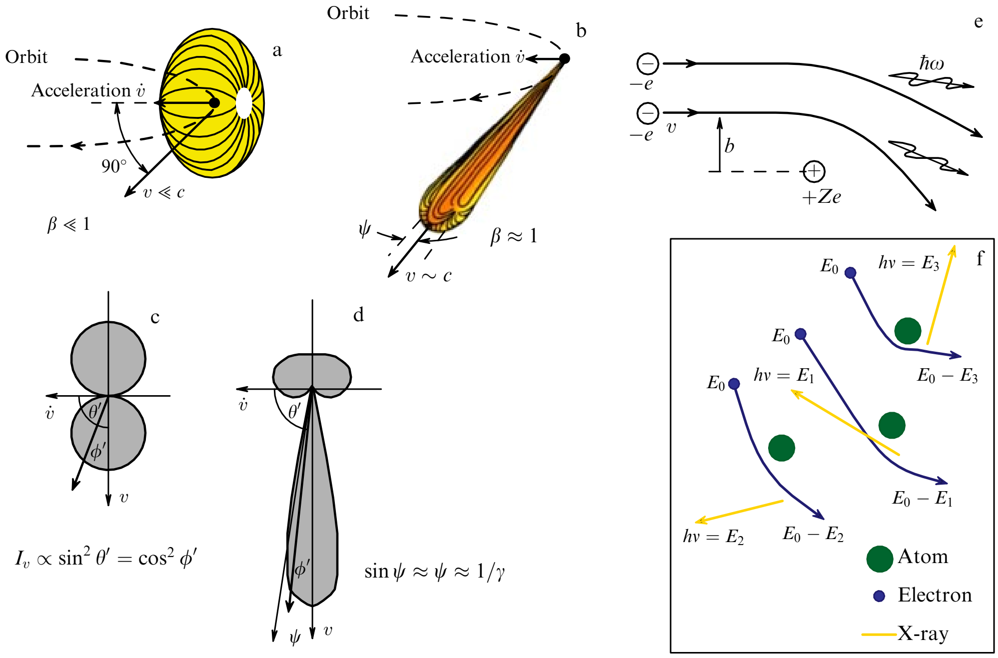

Figure 4. Spatial distribution of the electromagnetic radiation of an electron moving under the effect of a bending magnetic field or atomic potentials in a circular orbit. (a) Nonrelativistic electron in a cyclotron; radiation intensity is distributed over a toroid with the axis oriented in the direction of acceleration. (b) Relativistic electron, radiation is concentrated in a narrow beam directed along the electron velocity vector. (c, d) Cross sections of respective spatial distributions (a, b) in the plane of the electron orbit. (e, f) Variation in the orbits of respective relativistic and slow electrons decelerated in the potential fields of atoms of a condensed medium with the emission of bremsstrahlung photons. b is the distance of the maximum approach of the incident relativistic electron to the nucleus of an atom or ion with a charge $+Ze$.

paths, the relativity theory laws are applied, where the relativistic Lorentz factor is of importance:

$$\gamma = \frac{1}{\sqrt{1-\beta^2}} = \frac{E}{m_0 c^2} \,. \tag{4}$$

The relevant notation is introduced at the beginning of Section 3.1. The Lorentz factor is the ratio of the energy of a relativistic particle to its rest energy and is a measure of the relativistic contraction as a function of the energy, due to which the electromagnetic radiation of the electron is concentrated entirely in a cone with the opening angle (Fig. 4b, d)

$$\sin\psi \cong \delta\psi = \sqrt{1-\beta^2} = \gamma^{-1} = \frac{m_0 c^2}{E} \,.$$

In most SR sources designed based on storage rings [34–36, 68, 73, 74], electrons are accelerated to energies of several GeV (for example, 6 GeV at the ESRF (European Synchrotron Radiation Facility) storage ring in Grenoble, France). The divergence of the SR beam at such an energy is very small ($\psi = 2/\gamma = 0.5$ mrad, or 0.028°). Because the cross section of the electron beam, which is the SR source, does not exceed tenths of a millimeter in modern storage rings such a small divergence, even without focusing, allows using nearly 100% of the SR photons of the required energy for irradiation in the diffractometer of a sample with a size of about 1 mm.

In operating an XRT whose radiation intensity is distributed in a spherically symmetric way, under the same conditions and without using state-of-the-art optical devices, which are discussed in Section 4 below, no more than $\sim 0.01\%$ of X-ray photons produced in the focus of the XRT anode reach the sample under study, as can be easily estimated by simple calculations. Given the quadratic dependence of the bremsstrahlung intensity on the energy of emitting electrons [11, 72] and the enormous superiority of the electron energy in the synchrotron over the electron energy in the XRT, the density of the SR flux in the area of the sample under study is at least several orders of magnitude higher than the photon flux density of both bremsstrahlung and characteristic radiation of a regular sealed XRT, as confirmed by the data displayed in Fig. 5.

A specific feature of the use of X-rays in XRD methods of XRSA in comparison with many other areas is that theoretical models of the diffraction process have to be developed and the required results then follow by comparing the model with the data of XRD measurements [50]. More accurate models yield more reliable results. The most important part of the mathematical model is the instrumental function [78, 79] and the correspondence of the employed radiation to the initial conditions of the theory, in the framework of which an analysis is carried out, for example, to the kinematic approximation of diffraction theory [3, 11, 12, 49, 60, 80]. To develop a correct model and obtain reliable results, it is necessary to know the main characteristics of the tool used and the characteristics of the radiation, for example, the path of the rays in the beam, polarization, and the intensity distribution. Many of these parameters are often unknown for radiation generated by XRTs; therefore, it is much more difficult to construct an exact model of the instrumental function for radiation from an XRT than for SR. Synchrotron radiation is in this sense the source that is the most ‘pure’ and suitable for mathematical simulation, very attractive for precision diffraction studies, and the technique of its application in practice is quite well mastered [34–36, 68, 81].

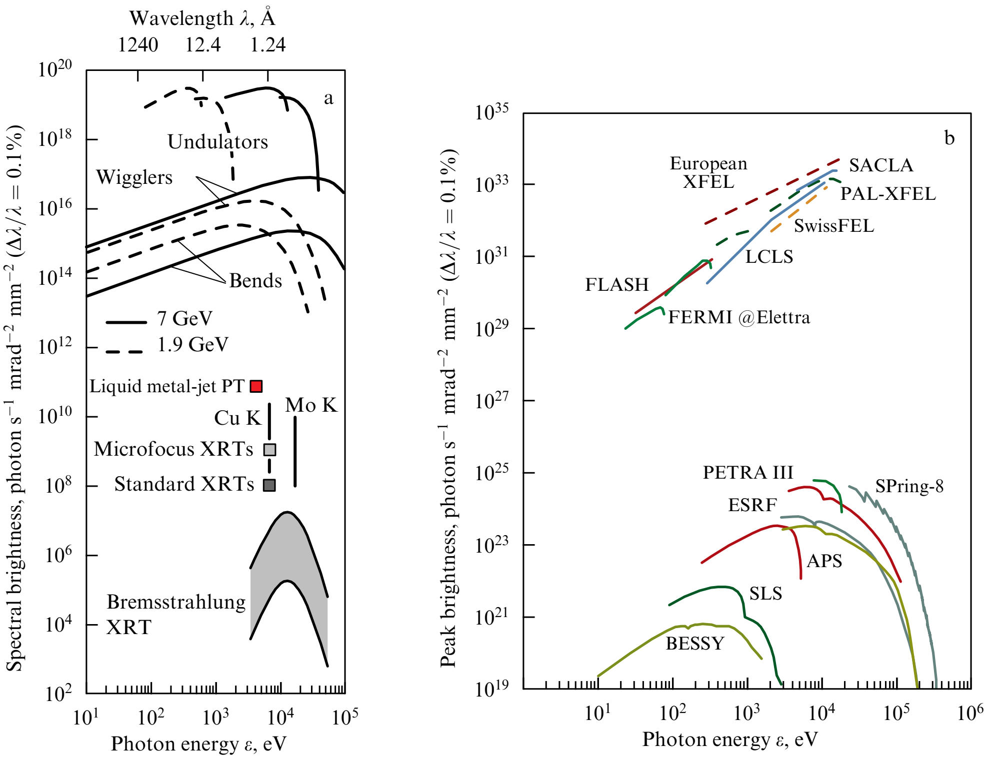

Figure 5. Comparison of the brightness of modern sources of X-rays. (a) Spectral brightness of some third-generation SR sources and laboratory XRTs. For storage rings with various electron energies (7 and 1.9 GeV), intrinsic spurious radiation from bending magnets (bends) and dedicated radiation from magnetic inserts, undulators, and wigglers are shown. For XRTs, vertical dashes denote the brightness of the characteristic radiation lines of standard rotating-anode tubes (Cu Kα and Mo Kα) of various powers; the squares indicate the brightness of the characteristic lines of a sealed tube with a fixed anode (standard XRTs), a microfocus tube with a fixed anode (microfocus XRTs), and a microfocus tube with a liquid metal anode (liquid metal-jet XRT) GaKα 9.25 keV (1.34 Å); bremsstrahlung is indicated as a shaded area where the lower boundary corresponds to fixed-anode tubes, the intermediate area to a standard rotating-anode XRT, and the upper boundary to a microfocus rotating-anode XRT (data compiled from publications [72, 75, 76]). (b) The maximum peak brightness of the most powerful operating sources of third-generation SR and X-ray free-electron lasers (XFELs) — fourth-generation SR sources (the names of the sources are indicated next to the spectra). The plot is taken from [77].

3.2 Sources of synchrotron radiation

Synchrotron radiation is by its nature strongly collimated along the direction of motion of the relativistic electrons that generate this radiation (see Fig. 5) and features a very high spectral brightness [60, 61, 67, 68, 70]. Dedicated SR sources were initially designed similarly to synchrotron storage rings used to study elementary particles, i.e., to cyclic resonant accelerators where the orbit of particles has the form of a flat closed polygon with radio-frequency accelerating stations located in the straight sections and high-power bending magnets in the corners. When an electron bunch passes through a bending magnet, a parasitic SR emerges [34–36, 60, 61, 70], whose pulses can be observed through a window in the storage ring, where the channels are arranged for collecting this radiation to be used in experiments. In addition to bending magnets, modern large-scale dedicated SR sources [74] contain many more specialized magnetic devices (wigglers and undulators) installed on straight sections of the electron beam orbit to create additional radiation channels. The principle of operation, design, and characteristics of SR sources are discussed in detail in many dedicated reviews, monographs, and textbooks, including some monographs on XRSA [4, 18, 33–36, 45, 60, 61, 67, 68, 70, 81, 82].

Three types of magnetic devices that bend the trajectories of relativistic accelerated electrons are used as sources in SR generators based on storage rings: (1) bending magnets, which ensure keeping the electron beam in a closed orbit of the storage ring; (2) wigglers, which are not characteristic of synchrotron storage rings, but are especially inserted in the straight sections of the storage ring; they are strong multipolar magnets with a zero total field that locally (in a small portion of the orbit) sharply bend the electron beam, forcing it to generate electromagnetic waves with a higher intensity and an energy higher than the radiation from bending magnets (see Fig. 5); (3) undulators, which are long linear arrays of permanent magnets located with a constant pitch that have alternating polarity and a much weaker magnetic field than the wiggler. The undulators make the electron beam follow a sinusoid when passing through the undulator and generate almost monochromatic radiation, whose wavelength can be adjusted by changing the distance between the poles of the permanent undulator magnets (for example, Fig. 5 shows tuning curves for several undulators). SR is in all three sources self-collimated and completely polarized, although in different ways [61, 67, 70, 83]. It is generated in dedicated sources in passing an electron bunch through the aperture of the radiation output channel in the form of a regular sequence of short pulses, i.e., it has a temporal structure that can be used for measurements with a time resolution reaching nanoseconds, and, in fourth-generation SR sources, even femtoseconds.

Construction of third-generation SR sources based on synchrotron storage rings began in the last decade of the 20th century in a number of countries [34–36, 60, 67, 68]. These new facilities feature optimized storage rings and a large number of SR output channels from magnetic insertion devices, with the brightness of individual emitters higher than 10^{20} photon s^{-1} $mrad^{-2}$ mm^{-2} $(\Delta\lambda/\lambda = 0.1\,\%)$, which greatly exceeds the brightness of the radiation of any XRT (Fig. 5). At the same time, bounds on the technological characteristics of these large-scale facilities have almost been attained. The point is that to keep the electron beam in orbit for a long time and maintain stability of the storage ring, a certain balance between the accelerator energy and the magnetic structure of the synchrotron is required, due to which the power and geometric parameters of the electron beam (the electron bunch size and the number of bunches in the ring) can only be varied within certain ranges.

In the storage rings of third-generation SR sources, the transverse size of the electron beam in the plane of the ring is usually about 150 μm, while the electron bunch has a horizontal emittance of about 2–3 nm rad and a duration of about 50 ps. The electron beam emittance [61, 72, 82], which depends on the root-mean-square transverse size of the electron bunch and the solid angle into which electromagnetic radiation is output ([34–36], Section 2.6.3), is the factor that determines the spectral brightness of a radiation source. A further enhancement of the brightness of the radiation, its transverse coherence, as well as a reduction in the time characteristics using synchrotron storage rings is extremely difficult, and a switching to alternative technologies is required.

3.3. X-ray lasers

Attempts to further increase the brightness of X-ray sources commenced at the beginning of the 21st century by means of powerful linear accelerators in combination with long undulators serving as generators of electromagnetic radiation, where the electron beam is used only once and therefore there are no restrictions inherent to the storage rings that hold electrons in orbit for a long time. The minimum diameter of the electron beam is only limited in linear accelerators by the diffraction limit. The normalized emittance is determined primarily by the characteristics of the electron gun, the length of the electron bunch being set by the compressor [84], and the typical values of these parameters achieved today in linear electron accelerators [85] are 0.03 nm rad and 100 fs. Hence, the beam in a linear accelerator can be many times brighter and the pulse hundreds of times shorter than in an electron storage ring. Based on the combination of a linear electron accelerator with an undulator, X-ray free electron lasers (XFELs) were designed and their construction commenced. A description of the operating principle, setups, and typical characteristics of facilities of this type can be found, e.g., in reviews [70, 71, 77, 82, 85–91] or in Section 2.9.1 of [34–36].

The main difference between synchrotron electromagnetic radiation, including that from undulators or wigglers installed on storage rings, and radiation from free electron lasers is that SR is emitted by electrons from the storage ring and its magnetic insertion devices in an incoherent way, i.e., each electron emits independently of the others, while FEL radiation is coherent: all electrons of the bunch emit synchronously. The intensity of radiation from the storage-ring undulator is therefore proportional to the number of electrons in the bunch, but in a FEL, to this number squared, and can therefore be billions of times higher than the intensity of spontaneous undulator radiation from storage rings (Fig. 5b).

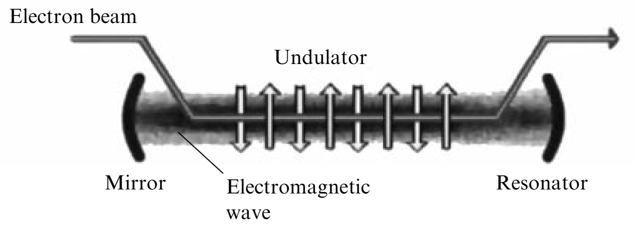

Figure 6. Principle of pumping a free-electron laser (FEL oscillator).

The mechanism for amplification of the intensity of electromagnetic radiation in FELs consists of the interaction and exchange of energy between quasimonochromatic electromagnetic radiation and well-structured bunches of ultrarelativistic electrons. Among the variety of FEL setups [87], two are distinguished that are commonly used in modern projects: the FEL oscillator [70] and the FEL amplifier [77, 85, 86] based on the self-amplifying spontaneous emission mode, SASE (self-amplified spontaneous emission).

The FEL oscillator setup is similar to that of an optical solid-state laser (see Fig. 6): it can be pumped in several passes of electron bunches through a long (about 5 m) undulator and does not therefore require too high an energy of ultrarelativistic electrons or a powerful accelerator once it has an ultralow emittance [90]. However, due to the need for resonator reflectors in FEL oscillators, it is very difficult to ensure the accumulation of short-wave electromagnetic radiation and its resonant interaction with the electron beam, making the task of tuning the wavelength in this system especially challenging. Therefore, such FELs are now successfully operating in the infrared (IR), optical, and ultraviolet (UV) ranges, but are not effective even for soft X-ray radiation, although there are ideas and prospects for improving the design of FEL oscillators to generate hard X-ray laser radiation [90, 92–94].

To generate laser radiation in the X-ray range, FEL amplifiers based on a linear accelerator (LINAC, for LINear Accelerator) with a high current and the SASE mode in a long undulator are primarily used now [85, 95].

In the SASE mode (Fig. 7), the effect of laser radiation is achieved with a single pass of an ultrarelativistic high-intensity electron bunch through a long undulator that amplifies its spontaneous emission by several orders of magnitude without the use of any optical resonator.

An FEL amplifier (in contrast to an FEL oscillator) uses a very high-energy electron beam with a current of several amperes (several kiloamperes per pulse) and a very long undulator (100 m or more). The powerful spontaneous undulator radiation of a well-compressed electron bunch, which emerges at the entrance to the undulator and is generated along the entire path through it, groups the electrons of the bunch by its oscillating electric field, like a radio-frequency resonator accelerator with autophasing (see Fig. 7), lining them up into thin layers of micrometer length and making them radiate in a coherent way.

On its way through the undulator, the electron beam sequentially goes through three modes of spontaneous emission (see Fig. 7): (1) spontaneous undulator radiation, (2) self-amplification of spontaneous emission as electrons are arranged and grouped; and (3) spontaneous-emission saturation. The electron bunch is broken at the exit from a sufficiently long undulator into thin plates of dense

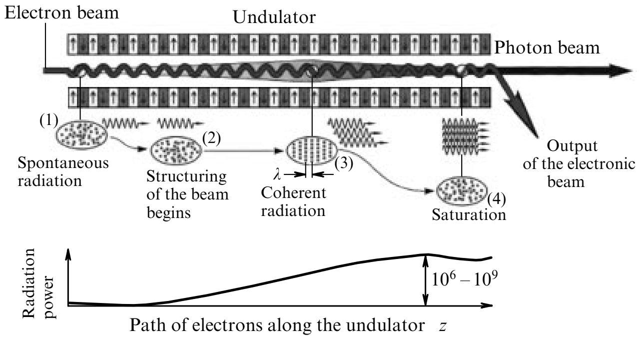

Figure 7. Operation of a resonator-free FEL amplifier in the SASE mode. The electron bunch at the end of its path through the undulator is split into microbunches under the effect of spontaneous emission of the electron bunches that follow this bunch. The electrons of the microbunches give off emission coherently with a total intensity (power) proportional to the number of electrons squared. The electron beam is dumped at the exit of the undulator into the absorber, and laser radiation is used for its intended purpose.

microbunches spaced apart by a wavelength, and all these formed microbunches radiate coherently at a specific wavelength. The radiation wavelength can be tuned by changing the accelerator energy and the magnetic field of the undulator [77].

XFELs are built based on linear accelerators designed for the electron energy $E = 5 - 20$ GeV with a large pulsed current ($I_{\text{pic}} \sim 3 - 10$ kA, $N_{\text{e}} \sim 10^{10}$, $l_{\text{bunch}} \sim 100$ μm). To date, several XFELs, sources of coherent radiation with brightness ten orders of magnitude higher (Fig. 5b) than the brightest sources of third-generation SRs, are in operation [34–36, 72, 91, 96, 97].

The first XFEL was the LCLS (Linac Coherent Light Source) commissioned in 2007, a 3-km-long X-ray laser at the SLAC (Stanford Linear Accelerator Center, Stanford, USA) [88], which operates on a standard LINAC with an energy up to 15 GeV and generates coherent radiation in the wavelength range $1.5 - 25$ Å in the form of pulses with a duration from 10 to 500 fs with a frequency of 120 Hz [77].

The second facility was the SACLA X-ray source (SPring-8 Angstrom Compact free electron LAser) commissioned in 2012, an unusually short (only 0.7 km long) Japanese XFEL [77, 89, 98, 99] at the linear accelerator of SR source SPring-8 (Japan) with an energy of 8.5 GeV. Owing to the use of vacuum undulators with a short period and high quality of the LINAC beam, this modest-length FEL generates laser-like radiation with an energy of 4 to 20 keV ($\lambda_{\min} = 0.6$ Å) with a maximum power of 6 to 60 GW in pulses whose duration is about 10^{-14} s. The SACLA pulse repetition rate is currently 30 Hz; however, it is expected that after upgrading it will increase to 60 Hz.

The third and world's largest SASE-mode X-ray laser is the European XFEL, commissioned in 2017 at the DESY research center (Deutsches Elektronen-SYnchrotron, Hamburg, Germany). It operates based on a superconducting LINAC with an energy up to 17.5 GeV and provides the wavelength range $0.5 - 60$ Å. This unique 3.4-km-long physical facility [91] operates in conjunction with the longest superconducting linear accelerator (1.7 km), which outputs dense bunches of ultrarelativistic electrons into several long undulators, where intense pulses of laser-like X-rays are generated for experiments. The radiation brightness of this giant device is 5×10^{33} photon s^{-1}mrad^{-2}mm^{-2} in a pulse ($\Delta\lambda/\lambda = 0.1$ %) (Fig. 5b). It produces ultrashort X-ray bursts with a frequency of 27,000 Hz and, as of 2018, is the world's most powerful source of coherent X-rays [96].

PAL (an abbreviation for Pohang Accelerator Laboratory), a 1.11-km-long XFEL (10 GeV, $\lambda_{\min} = 1.0$ Å) began operations in 2017 in the Republic of Korea.

The overall situation with SR sources and X-ray lasers in the world as of the end of 2006 was presented in the summary Table 6.12 of book [34–36] and in Sections 2.8 and 2.9 therein. The number of SR sources in the world has not changed much in the 11 years since this book was published. Some obsolete synchrotrons were decommissioned, and almost all the installations marked in the table as being under construction have been put into operation. They are six third-generation SR sources based on large storage rings that are located in Australia (Australian Synchrotron with a 3 GeV ring), England (DIAMOND (DIpole And Multipole Output for the Nation at Daresbury), 3 GeV), France (SOLEIL (Source Optimisée de Lumiére d'Énergie Intermédiaire du LURE), 2.75 GeV), Germany (PETRA III at DESY Research Center, 6 GeV), Jordan (SESAME (Synchrotron-light for Experimental Science and Applications in the Middle East), 2.5 GeV), Spain (ALBA, 3 GeV), China (Shanghai SSRF (Shanghai Synchrotron Radiation Facility), 3.5 GeV), and Taiwan (Taiwan Photon Source, TPS, 3 GeV). The design of the third-generation Iranian SR source with a beam energy of 3 GeV (Iranian Light Source Facility (ILSF)) in Tehran has commenced.

Twelve various FELs were under construction and customization during this period, many of which are designed for radiation in the hard X-ray range, and four (Fig. 5b) have already been commissioned [96] and are delivering femtosecond pulsed coherent radiation for experiments. As can be seen from Figs 8 and 5b, the construction of the XFELs over one decade of the 21st century enabled enhancing the brightness of X-ray sources by almost 10 billion times compared with those sources that were developed and built over the previous 120 years.

The radiation provided by SR sources and XFELs meets the most demanding requirements of X-ray users. But these facilities exhibit a significant disadvantage: their dimensions are very large and the construction and operating costs are truly immense. The construction and operation of such facilities usually require multimillion dollar expenses, due to which they are not feasible without the involvement of government (or several governments). For example, the cost of constructing and commissioning the European XFEL, in which more than a dozen European countries participated [96, 100], was as high as 1.22 billion euros (in 2005 prices), of which 27% was provided by the Russian Federation as one of the project participants.

The number of SR sources worldwide is only slightly more than 50 and is increasing slowly. They are experimental resource-sharing facilities with selectively limited access and, as a rule, cannot be used to rapidly solve academic and engineering problems. Therefore, the search for more affordable alternative radiation sources with user characteristics similar to synchrotron radiation or X-ray laser radiation is in progress.

3.4 Alternative X-ray sources

Alternative sources of high-brightness radiation with attractive user properties, but less bulky, less expensive, and more easily accessible to users have been developed in the last two or

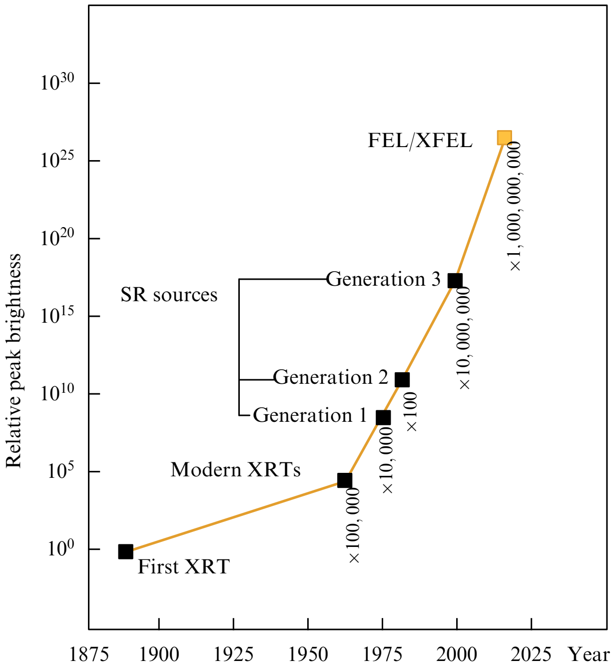

Figure 8. Historical progress in the brightness of X-ray sources from the time when Röntgen published his discovery to the present day. Comparison of the peak brightness of various X-ray sources up to free electron lasers in SASE mode (European XFEL, 2017) with the brightness of the first XRT (1885). (The plot is taken from [91].) The numbers indicate the factor by which the brightness of the next-generation sources differs from that of the sources of the previous generation.

three decades, in addition to building new SR sources based on storage rings and XFELs based on giant linear accelerators. A description of these developments can be found, e.g., in Section 2.9.4 of [34–36] and in [62, 63, 101–106]. These promising sources most often operate based on the interaction between relativistic electrons and condensed matter of various types, in which bremsstrahlung or X-ray range fluorescence radiation [103, 106] and, in some cases, transition and parametric radiation [62, 104, 107] are generated. These developments in most cases fail to go beyond the stage of prototypes, but even those that have reached the standards of a commercial product have not yet won a significant share of the global market for X-ray sources, which is dominated by XRTs and synchrotron sources.

An instructive example of the design of an alternative X-ray source with properties similar to SR, which was brought to the level of a commercial product, is the series of compact MIRRORCLE radiation sources that generate hard electromagnetic radiation. MIRRORCLE is a new type of X-ray source based on a compact cyclic electron accelerator that generates pulsed radiation with characteristics similar to those generated by a large-scale synchrotron or radiation from an XRT. These sources are designed and manufactured by Japan-based Photon Production Laboratory, Ltd. [106], which in 2014 [108] produced four models of the device with electron energies from 1 to 20 MeV (1, 4, 6, and 20 MeV) for use in various enterprises ranging from mechanical engineering and materials science to medicine.

The design and technological characteristics of these devices are described by their authors and designers [106, 109–111], and general information about them can be found in Section 2.9.4 of [34–36]. These small-size installations use the X-ray generation method based on interaction between a beam of ultrarelativistic electrons and a solid. MIRRORCLE consists of an electron injector, a microtron accelerator, and an ultra-small-diameter synchrotron storage ring (ranging from 0.65 to 130 cm, depending on the electron energy [108]), with a solid-state target mounted in the path of the electron beam.

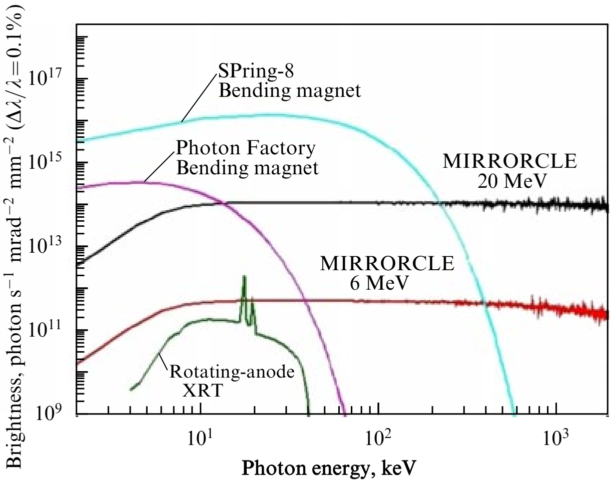

Figure 9. Comparison of the radiation brightness of laboratory pulsed MIRRORCLE sources of two modifications (electron energy 20 and 6 MeV) with the brightness of rotating-anode X-ray generators and the brightness of SR from bending magnets of Japan-based large storage rings (Photon Factory and SPring-8). (According to the data in [109].)

Despite the relatively modest size, a total weight of less than 3 tons for the most powerful version, and the possibility of installation in a facility with an area of about 20–30 m^2, these sources can generate pulsed radiation in the range from hard ultraviolet (EUV: Extreme Ultraviolet) to hard X-ray radiation (Fig. 9), with a brightness comparable to radiation from bending magnets of third-generation SR sources [108, 109], and output it to users via several channels.

Section 2.9.3 in [34–36] and publications [112, 113] provide examples of the so-called Thomson laser–electron sources of X-rays that generate bright quasimonochromatic radiation using the inverse Compton scattering of an optical laser beam on the colliding beam of ultrarelativistic electrons in small cyclic or linear accelerators. These sources generate X-rays in the collision of relativistic electrons with IR laser photons. This method in principle allows creating a rather compact source of pulsed X-ray radiation by combining a terawatt IR laser with an electron accelerator and/or small-size synchrotron with an energy of several dozen MeV [114, 115]. For example, a small-size Compton laser source of this type commercially manufactured in Germany under the tradename MuCLS (Munich Compact Light Source) [113], which can easily be housed in a laboratory hall with an area of about 150 m^2, emits a radiation beam whose intensity, geometry, polarization, and time characteristics are close to those of the radiation from a bending magnet in a third-generation SR source, which is easily described and mathematically modeled, in contrast to radiation from an XRT. The power consumption of this installation (about 80 kW) is comparable by the order of magnitude to the most powerful X-ray generators with a rotating anode. According to the estimates made in [113], the brightness of the MuCLS source is 4.8×10^9 photon s^{-2} $mrad^{-2}$ mm^{-2} ($\Delta\varepsilon/\varepsilon = 0.1\%$) for X-rays with an energy of 25 keV.

3.5 Laser plasma X-ray generators

Among alternative sources of bright X-rays, the development of laser–plasma (LP) X-ray sources has been especially active over the past two decades [95, 116, 117]. The LP method of X-ray generation is already giving the shortest pulsed X-rays (duration from tens of femtoseconds to an attosecond), whose intensity is comparable to that of third-generation SR sources (Fig. 10).

The LP method is especially attractive for researchers because in the near future it can potentially ensure the construction of small-size linear electron accelerators with energies of up to tens or even hundreds of GeV and the development of compact XFELs on their basis [71, 118–130] (see, e.g., the EuPRAXIA[1] project 1 in [118] or information about this project published on the Internet at http://www.eupraxia-project.eu/).

An XFEL station of this type could be deployed and operated in a standard university laboratory or at some institution, for example, in a hospital. A point short-pulse high-brightness X-ray source in LP X-ray generators is the microplasma created by the local impact of a light pulse from a powerful optical laser on a target [132–136] (Fig. 11), for which both solid and liquid or gas can be used.

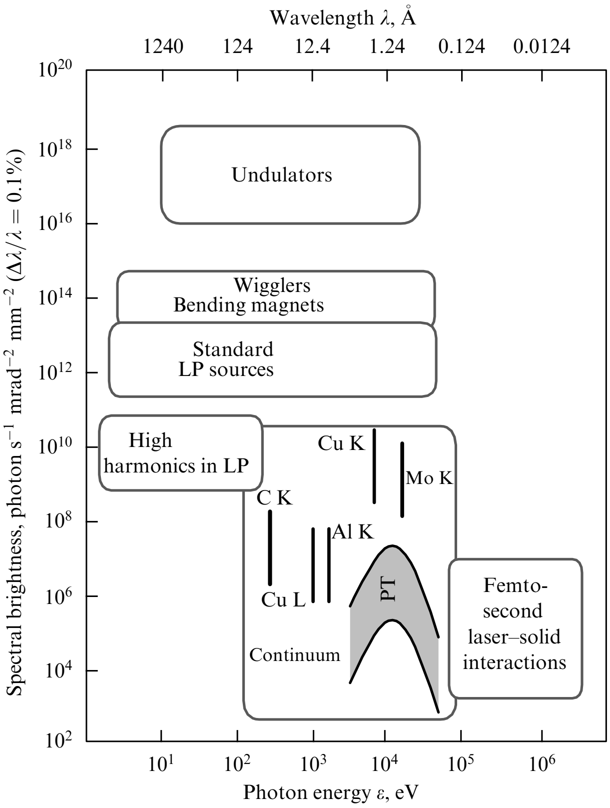

Figure 10. Comparison of the average spectral brightness of SR sources, standard XRTs, and LP X-ray sources, including data from recent experiments with ultrashort pulses, "Femtosecond laser–solid interactions." Data are taken from [131]. The area of standard LP sources corresponds to the radiation of a plasma source typical of the mid-1990s with a metal target (W or Au) irradiated by a laser with an average power of 100 W, with a pulse of ~ 1 J, ~ 10 ns at a repetition rate of ~ 100 Hz. The areas of radiation of undulators, wigglers, and bending magnets refer to well-known SR sources of the same times, such as ESRF (Grenoble, France), ALS (Advanced Light Source, Lawrence Berkeley National Laboratory, USA), and NSLS (National Synchrotron Light Source, Brookhaven National Laboratory, USA).

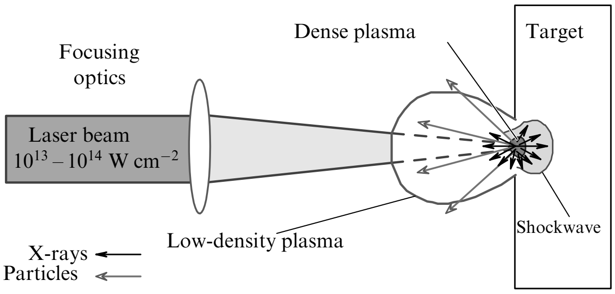

Figure 11. Diagram showing how plasma is produced under the effect of a laser pulse on a solid-state target. The emerging plasma emits various accelerated charged and neutral particles (gray arrows) and X-rays (black arrows).

To generate X-rays using LP, it is necessary to apply the short-pulse radiation of an optical laser with the pulse intensity (power density) $> 10^{16}$ cm^{-2} to the target. State-of-the-art laser technologies [129] allow satisfying this condition: when focused in a small region, they provide a laser pulse intensity above 10^{22} W cm^{-2} (Fig. 12).

The LP method of generating X-rays cannot be called completely new. Long-standing attempts [137–139, 140, 141] to produce and apply in practice pulsed X-ray radiation from plasma, including that generated by a laser, are known. Moreover, the existing experimental facilities for the generation of X-ray pulses by means of LP were manufactured and used in XRD studies [139] already in the early 1970s, i.e., when the first dedicated sources of synchrotron radiation only existed in projects.

Attempts were made at that time to use bright short-pulsed LP X-ray sources to obtain clear instant X-ray patterns of pulsating biological objects in medicine and biology (heart, lungs, etc.), as well as for X-ray spectral and X-ray structural time-resolved measurements [140]. However, for the next few decades, SR sources based on large cyclic electron accelerators [34–36, 67, 71], despite their large dimensions and high construction and operation costs, were significantly more developed and widely used than LP X-ray sources. This balance among various technologies persists in our time, although there are reasons to expect that it can soon shift in favor of LP technologies [118, 128, 130].

The development of LP sources was hindered primarily by the insufficiently high technological characteristics of the available optical lasers [102, 103, 119, 136, 142–144]. Interest in LP sources of ultrashort pulses of intense X-ray radiation returned by the beginning of the 21st century and began to grow rapidly [65, 95, 101] due to an increase in the need for structural and spectral studies of substances with picosecond and femtosecond time resolution [95, 145–147] and new achievements in laser technology made by this time (see Fig. 12) [119, 121, 125, 130]. To date, high-power short-pulse (picosecond and femtosecond) optical lasers (with a multi-terawatt or even petawatt power) have been developed that are suitable for powering such laboratory LP sources of short-pulse X-ray radiation whose brightness is comparable to that of SR sources of the newest generations [122, 125, 129, 148, 149]. The main attractive feature of LP X-rays sources is

---

[1] The name of the EuPRAXIA project, which sounds similar to the female name Eupraxia (prosperity in Greek), is actually an abbreviation for "European Plasma Research Accelerator with eXcellence In Applications."

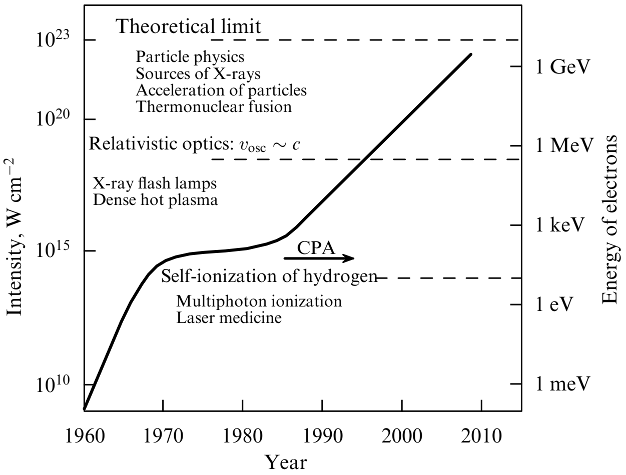

Figure 12. Growth of the achievable peak intensity (power density) of laser pulses since the invention of the laser in 1960. The dashed lines divide the plot of intensity into areas that differ significantly in the properties of radiation and the corresponding types of plasma. $v_{\rm osc}$ is the velocity of electron oscillations in the laser radiation field. Some important technological applications of lasers with the corresponding intensity are indicated in the selected areas. CPA (chirped pulse amplification) is a technology for producing high-power short laser pulses. (Plot is taken from [136].)

that they are tens and hundreds of times more compact than SR sources based on storage rings and are much less expensive, which implies that they are more affordable for researchers. These sources made the prospect of studying dynamic processes feasible in academic laboratories or in manufacturing environments rather than in barely accessible SR centers. Finally, owing to recent advances in laser technology (see Fig. 12), opportunities have emerged to experimentally implement a number of ideas already developed in relation to laser plasma, in particular, to create miniature multi-GeV laser accelerators of electrons and, based on them, compact XFELs [118, 119, 124–126, 129, 130].

3.5.1 Laser plasma: properties and generation of X-rays. Laser plasma is an unsteady plasma medium produced due to the ionizing effect of high-power laser radiation on matter [67, 103, 126, 136, 142, 143, 150, 151]. It consists of a mixture of high-energy (up to relativistic energies) electrons and completely or partially ionized atoms, the mixture being electrically neutral as a whole. The LP is obtained as a result of optical breakdown, for example, in gaseous media (laser spark). Optical breakdown accompanied by the emergence of LP occurs if the target is exposed to a laser pulse of electromagnetic radiation with the power density $\phi \approx 10^{11}$ cm^{-2} in the case of a gas at atmospheric pressure or $\phi \approx 10^8 - 10^{11}$ W cm^{-2} for the evaporation and laser breakdown of solid target vapors (see the diagram in Fig. 11).

The spectrum of electromagnetic radiation of LP is very complicated in what concerns energy composition [67, 131, 140, 152, 153], propagation geometry, and polarization due to the variety of mechanisms that contribute to its formation. Electromagnetic plasma radiation is formed primarily by electron interactions [67, 131] between (1) free electrons and free electrons, (2) free electrons and bound electrons, and (3) bound electrons and bound electrons. The contribution of each mechanism to the emission spectrum depends on the plasma temperature and target type. In the first mechanism, rapidly moving free electrons interacting with the Coulomb potential of plasma ions emit a continuous spectrum of electromagnetic radiation, which yields so-called bremsstrahlung. The second process, known as recombination, consists in transitions of electrons from the initial free states to bound states; it also creates a quasicontinuous electromagnetic spectrum. The third radiation mechanism yields a linear spectrum as a result of transitions between discrete (bound) levels of ionized atoms. If the plasma is knocked out of a solid target, then some of the electrons flowing away return to this target and, in addition to their own radiation, start emitting bremsstrahlung and generating spectral lines of characteristic radiation corresponding to chemical elements of the target, as in X-ray tubes. We note that the type and intensity of the electromagnetic radiation of LP depends on the pulse intensity and wavelength of the exciting laser, as has been shown, for example, in [134, 154]. The spectral characteristics of LP X-ray sources can be varied by changing the atomic number Z of the target material [131].

The mode of radiation generation by LP is conventionally divided into the 'high-intensity' and 'ultrahigh-intensity' regimes [154]. The onset of the high-intensity regime occurs, for example, at laser-pulse intensities ranging from 5×10^{14} to 10^{18} W cm^{-2} at a wavelength of 1 μm. The regime with an intensity $\phi > 10^{18}$ W cm^{-2} is an ultrahigh-intensity one, and the LP formed under its effect is relativistic because the electrons it contains gain relativistic energies. The threshold of the laser intensity necessary for the plasma to switch to the relativistic regime actually depends on the wavelength; the longer the laser wavelength, the lower power is required to excite the relativistic regime. For example [130, 154], for an excimer laser with a wavelength of 248 nm, the relativistic transition occurs at an intensity of 10^{19} W cm^{-2}, while for a laser with a wavelength of 10.6 μm (CO_2 laser) this threshold is observed at a much lower intensity of 10^{16} W cm^{-2}.

The development of laser technology and nonlinear optics [125, 154, 155] by the end of the 20th century (see Fig. 12) has led to the emergence of laser systems of relatively small dimensions that easily reach the level of ultrahigh intensity, i.e., emit focused pulses with intensities $\phi > 10^{18}$ W cm^{-2} that create a relativistic plasma. For example, ultrashort laser pulses with a duration of less than 10 fs and an energy of the order of 1 mJ, if focused onto a spot whose size is equal to one wavelength, can produce intensities above 10^{18} W cm^{-2}, thus forming a plasma with a relativistic regime of radiation generation [154, 156].

Laser-plasma X-ray generation is represented by two completely different methods [101, 116].

(1) generation of higher harmonics (laser high harmonic generation or HHG method) [157] that consists of converting the frequency of the radiation from the feed laser to higher harmonics (the wavelength of the laser pulse is contracted many times when passing through a plasma channel, usually in a gaseous medium); for example, laser IR radiation at certain parameters of the pulse and the gas medium can have a higher harmonic with the wavelength in the X-ray region [67, 158], while the radiation remains coherent;

(2) emission by electrons and ions of a hot dense plasma, which is triggered by a radiation pulse from the feed laser (the initial laser radiation is converted into heat, while X-rays are emitted by excited particles of the resulting plasma); the X-ray radiation is not emitted in this mechanism by the laser itself but comes from a hot plasma created by the effect of a laser pulse on the matter [131, 136, 159]; therefore, the radiation is incoherent and has a complex spectrum.

The basics of the theory and practice of the HHG method and its current state are discussed, e.g., in [67, 101, 116, 125, 131, 157, 158]. Method 1 is quite easily implemented by transmitting a focused long-wavelength laser beam through a capillary filled with an inert gas of reduced pressure [67, 95, 131, 157]. Not only is the radiation wavelength shortened in this case, but also the laser pulse is compressed in time, reaching attosecond durations. The HHG method is of interest because the coherent radiation of the feed laser is converted into radiation of the highest harmonic that is also coherent. In addition, the implementation of the HHG mechanism does not require an extremely high intensity of laser radiation; usually, higher harmonics are generated at laser intensities below 10^{16} W cm^{-2} [116, 154, 157]. However, so far, only wavelengths of vacuum ultraviolet and soft X-ray radiation with a maximum photon energy of the order of 1–2 keV have been attained using this mechanism. Therefore, the HHG method is not very suitable for XRSA of materials and chemicals because XRSA usually employs significantly harder radiation: X-rays with a wavelength in the range from 0.1 to 2.5 Å (energy from $\sim$ 5 to $\sim$ 124 keV).

Hard X-ray radiation suitable for applications in XRSA is usually generated in LP techniques by methods of type 2, like the radiation of a laser hot plasma. To obtain a laser plasma that can yield X-rays, laser radiation of extremely high intensity is required, much higher than that used in the HHG method. The spectral lines of characteristic X-rays are obtained in plasmas produced by laser pulses with the intensity not less than 10^{16} W cm^{-2}, while to obtain sufficiently intense bremsstrahlung radiation with the photon energy in the X-ray range, a laser power of more than 10^{17} W cm^{-2} is required [116, 131, 135, 152]. Such immense intensities of light can be achieved in small volumes by compressing a reasonable amount of light energy in an ultrashort and perfectly focused laser pulse [154]. For example, typical state-of-the-art commercially available laser systems can deliver about 5 mJ of light energy per pulse with a duration $\leqslant$ 50 fs on a spot with a diameter of $\sim$ 10 μm, a value sufficient to ionize the internal electron shell of atoms and generate characteristic X-ray radiation. The duration of the obtained 'monochromatic' pulses of X-ray characteristic radiation depends on the maximum depth of penetration of high-energy plasma electrons into the target [116].

There are many designs to construct LP generators of electromagnetic radiation. A typical schematic diagram of the design of an LP X-ray source is shown in Fig. 13 [160, 161].

In the simplest version, to generate X-rays using the LP method [95, 101, 103, 131, 143], a sufficiently powerful and short (nanosecond, picosecond, or even shorter) laser pulse focused on a spot about 10 μm in diameter is applied to a metallic target; it causes evaporation of matter from the target surface, the electro-optical breakdown of the generated vapor, and the formation of a short-lived microplasma [67, 136, 150, 151] with a high density and high kinetic energy of electrons.

To generate LP X-rays, lasers with pulses with a duration of 10^{-13} to 10^{-9} s and an energy of several dozen joules focused onto a spot with a diameter of 10–100 μm are typically used. Under these conditions, a microscopic plasma X-ray source with a total brightness of the order of 10^{17} W cm^{-2} sr^{-1} is obtained, whose peak brightness in the spectral band with a width of 0.01% can be as high as 10^{19} photon s^{-1} mrad^{-2} mm^{-2} [131], i.e., can exceed the radiation brightness of XRTs and is close to the brightness of SR sources [72], as can be seen in Fig. 10. The LP X-ray sources usually have the radiating area size less than 100 μm, an ultra-small duration of pulses [67], and extremely high brightness [52], as a result of which they are used rather frequently in practice for time-resolved XRD studies [101].

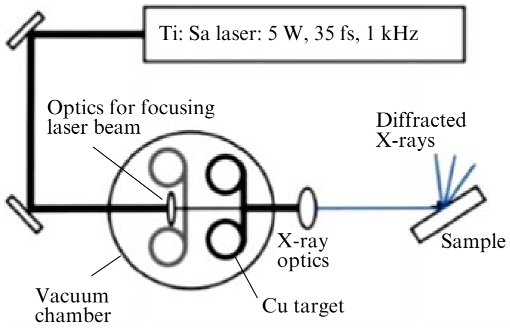

Figure 13. Setup of an experimental LP X-ray source for XRD measurements [160, 161]. Plasma is excited by a titanium–sapphire IR laser (wavelength of about 800 nm) with a pulse duration of 35 fs. Rewinding the target (a 20 mm thick copper tape) provided an unexposed and undamaged surface for each laser shot and ensured high stability of the X-ray source. The laser beam was focused on the target onto a spot about 10 μm in diameter, creating a light intensity of about 10^{18} W cm^{-2}. The X-rays generated from the focus were monochromatized and collected by an X-ray optical system (focusing Montel mirror) located in front of the sample, directed to the sample and recorded after diffraction by a coordinate-sensitive detector. According to measurements in [161], this source emitted 4×10^{10} photon s^{-1} with Cu Kα energy (8.04 keV) into the full sphere of 4π steradians, and X-ray optical elements were used to select $\approx 10^6$ photon s^{-1} from this flux and deliver them onto a spot less than 200 μm in diameter located at the position of the test sample.

We note that a device similar to that shown in Fig. 13 was also used to generate X-rays in a much older study [139]. The LP generator was powered in that study by a neodymium laser. First, in order to evaporate and ionize the material near the target surface, a short preliminary laser pulse with an energy of 1 J and duration of 10 ns, focused onto a spot with a diameter of 100–200 μm, thus ensuring a power density of 10^{11} W cm^{-2}, was applied to the surface. Next, the laser hit the produced low-temperature plasma with the main pulse ($\sim$ 100 J, 1 ns), delivering a power density of 10^{14} W cm^{-2} on a spot of the same size, 100–200 μm. X-ray radiation from the plasma was obtained in this case as a result of processes such as deceleration of high-energy electrons in the plasma, recombination of plasma ions, and the linear characteristic radiation of atoms of the solid target bombarded by fast plasma electrons.

In some cases, liquids [64, 162] or molten metal are used as the target of LP X-ray sources. For example, in [152], the target consisted of liquid mercury, which is not damaged by the laser, does not contaminate the surface of the vacuum chamber or the optical system with laser ablation products, and allows the source to function in a stable manner for a long time.

Sometimes used as master oscillators in pulsed LP X-ray sources for time-resolved X-ray studies [64, 95] are powerful titanium–sapphire IR lasers (wavelength of about 800 nm) with 30–50 fs pulses that are repeated with a frequency of 1 kHz [152, 160, 161, 163] (see Fig. 13).

In practice, lasers are sometimes used to generate LP X-rays whose power is thousands of times greater than that indicated in Fig. 13, such that the radiation brightness shown in the diagram in Fig. 10 can be attained. For example, in experiments to generate LP X-rays at the Laser Center of the Rutherford–Appleton Laboratory (England) [164], a group of researchers used a powerful Vulcan petawatt laser with pulses 0.9–1.2 ps in duration and an energy of about 80 J, focused onto a spot 10 μm in diameter on a tantalum foil target located in a vacuum chamber. LP electrons decelerating in the target generated X-rays and even gamma rays in this experiment.

Laser–plasma sources today can produce the shortest (down to attoseconds) pulses of X-ray radiation [95]. The duration of the X-ray pulses generated by LP sources is determined not only by the duration of the laser pulses but also by the laser energy and the target thickness [152]. If the target is of the order of 10 μm in thickness, the characteristic X-ray radiation excited by the electrons of the laser plasma lasts about 100 fs even if the laser pulse duration is 30–50 fs.

As regards the efficiency of the conversion of laser energy into X-ray radiation in LP generators, already the first attempts to use this radiation in practice showed that it depends on a number of factors not always related to the laser power, the medium, or the target material. For example, a preliminary plasma-stimulating laser pulse [139], which precedes the main powerful laser impact on a solid target, can increase the intensity of X-ray radiation by several orders of magnitude [161, 165]. Owing to the preliminary pulse, it was possible to obtain [139] the conversion efficiency of about 25%. This estimate apparently refers to the total intensity over the entire range of the X-ray spectrum, while the efficiency of converting the laser pulse energy into a linear characteristic radiation, as in XRTs, proves to be much lower (for example, about 10^{-5} in [103, 161, 166] or 10^{-3} in [167]) simply because of the special physical nature of the emergence of radiation of this type. It was found in [141] that in LP sources with targets of elements whose atomic numbers are about 30, roughly a quarter of the absorbed energy of the laser pulse can be converted into X-ray radiation, a value consistent with the data in [139].

The efficiency of using X-rays from regular LP sources is approximately the same as when operating the XRTs that were discussed above. The X-ray pulse emitted by the plasma discharge is isotropic, i.e., has no directionality and is evenly scattered into a solid angle of 4π srad. Therefore, even if the most wide-angle collimators are used, for example, Kumakhov polycapillary lenses with a beam capture angle of more than 20°, which are discussed below in this review, the collected radiation is only a fraction of a percent of about the 10^9 X-ray Kα photons emitted per pulse by the LP source with a solid target. The rest of the radiation is scattered in space, and half of it is absorbed by the target. However, the problem of increasing the X-ray source efficiency is solved in the case of LP generators much more easily than in XRTs. A way to increase the efficiency of LP X-ray generators and to almost completely use the photons generated by those generators is to switch the generation process to the relativistic mode, where the effect of self-collimation of electron radiation occurs, as was shown in the discussion of SR sources in Sections 3.1 and 3.2 of this review.

The radiation emitted by relativistic electrons, in accordance with the relativistic Doppler effect, is concentrated along the direction of motion of the radiating charge and self-collimated in a cone with the opening angle $1/\gamma$, where γ is the Lorentz factor (4). As a result of such directivity of radiation from relativistic sources, for example, the brightness of synchrotron radiation beams is many orders of magnitude higher than that from XRTs. It turns out that by switching to the relativistic mode it is also possible to increase the efficiency of using radiation and LP sources, and at a much lower cost than if switching from XRTs to SR from storage rings.

3.6 Laser-plasma accelerators and free-electron X-ray lasers

It was noted at the beginning of Section 3.5 that the main reason for the general interest in LP methods for X-ray generation is the prospect of using this method to create miniature X-ray lasers to replace the giant XFEL systems under construction today, as discussed in Section 3.3. The theory and practice of LP acceleration of electrons to ultrarelativistic energies has been actively discussed over the past three decades [119, 121, 124–126, 129, 130, 131, 156, 168–170], along with the prospects of using these physical principles for the creation of future 'desktop' XFELs and compact accelerators and colliders with energies above 100 GeV.

Almost forty years ago, in 1979, Tajima and Dawson [168] proposed and justified the method of LP acceleration of electrons (Laser Wake Field Acceleration: LWFA) to relativistic energies by using the field of a relativistic plasma wave generated in the wake of an intense laser pulse passing through the plasma. However, for this elegant idea to be implemented in practice at that time, there were no technological means that could produce laser radiation of the required quality (pulses of duration < 100 fs with the intensity $> 10^{17}$ W cm^{-2}). Such means were created in the late 20th century [126, 130, 136, 154] and became available later; at the beginning of the 21st century, scientific and technological developments and projects for the construction of LP accelerators and X-ray lasers based on them were actively promoted [102, 118, 122, 123, 126–130, 170, 171].

Of the variety of mechanisms of LP acceleration of charged particles [124], the most developed and most commonly used is currently a setup based on acceleration by the electric field that emerges as a result of spatial separation of ions and electrons in a plasma. In the LWFA mechanism of acceleration of electrons proposed by Tajima and Dawson [168], the LP interaction occurs in the relativistic mode, when a plasma wave is excited by a laser pulse with an intensity $\geqslant 10^{18}$ W cm^{-2}. In switching to the relativistic regime in laser radiation, the role of the magnetic component of the electromagnetic wave significantly increases [124], and the ponderomotive force associated with it increases to a level sufficient to push electrons out of the high-intensity pulse region. For example, at an intensity of 10^{19} W cm^{-2} at a wavelength of 1 μm, the ponderomotive potential is 1 MeV [126]. In this mode, the light pressure of the laser pulse displaces all plasma electrons from the high-intensity zone, but does not actually displace heavy ions. As a result of such separation of charges in the plasma, a strongly positive-charged cavity ('bubble') is formed near the laser pulse, which, like a wake wave, follows the laser pulse moving at the speed of light and drags adhered plasma electrons after it (Fig. 14).

This wake wave generates a longitudinally moving electric field behind the laser pulse in the plasma [124, 156, 168], which forms a steep accelerating gradient, which for typical plasma electron densities ($10^{18} - 10^{19}$ cm^{-3}) can be greater than 100 GV m^{-1}, exceeding the permissible accelerating voltage of the radio-frequency accelerating resonators of

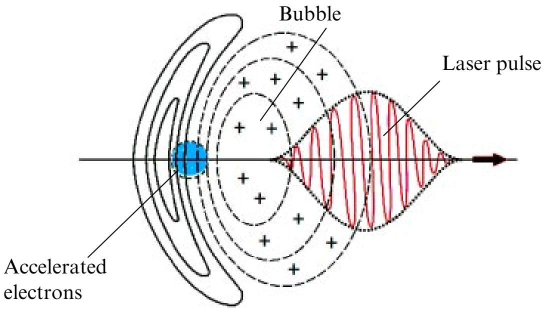

Figure 14. The LWFA mechanism of electron acceleration by a plasma wake wave from a laser pulse. The diagram shows how a laser pulse of relativistic intensity propagates in plasma. An electron-free cavity (bubble) filled with positive ions is formed in the wake of the pulse, which, following the pulse, draws and accelerates the 'sticking' plasma electrons by an extremely strong electric field.

standard electron accelerators by 3 to 4 orders of magnitude [125, 156].

Electrons can be accelerated by the LWFA mechanism to 1 GeV at millimeter or centimeter distances [120, 124], while it takes several dozen of meters to reach the same energy in standard accelerators. To accelerate electrons to energies of tens of GeVs using regular radio-frequency resonators, accelerators many kilometers in length have been built [88, 91].

The force created in a plasma by light pulses with ultra-relativistic intensity has already been repeatedly used to accelerate electron beams to MeV energies at micrometer distances [156] and to several GeVs in a plasma channel several centimeters in length [102, 120, 122, 123, 125, 127]. Simulations [122] show that using the currently available laser technology, the electron beam can be accelerated in a plasma channel about 1 m long at a plasma density of 10^{17} cm^{-3} to an energy of 10 GeV by laser pulses with a duration of 50–200 fs and an energy of 30–40 J, focused to a diameter of 50–100 μm. For example, using LWFA technology in a 9 cm plasma waveguide, specialists from the Lawrence Berkeley National Laboratory (California, USA) demonstrated a setup that allowed creating a high-quality 4.2 GeV electron beam [123], which is usually obtained in giant synchrotrons that are larger than the football pitch. This result was achieved due to the optimization of experimental parameters, especially the state and density of the plasma, which ensures the passage of the laser pulse along the entire length of the capillary.

3.7 Prospects for free-electron X-ray lasers based on a laser-plasma accelerator

It was shown about 10 years ago that collimated short-pulse ($\sim$ 10 fs) undulator radiation can be obtained from electron beams accelerated by the LP method [172]. The experiment was carried out at a relatively low LP acceleration energy and with a rather short undulator. The accelerator 1.5 cm in length provided an electron beam with the energy $\sim$ 210 MeV. When passing through a 30-cm-long undulator, this beam generated electromagnetic radiation that consisted of two peaks of undulator radiation and a peak of the short-wavelength edge (the main peak at the wavelength $\sim$ 18 nm, the second harmonic peak at $\sim$ 9 nm, and the high-energy edge at $\sim$ 7 nm). This radiation was, of course, a very soft X-ray one and was not coherent. However, this experiment for the first time showed a realistic possibility of creating an XFEL generating sufficiently hard X-ray radiation based on a high-energy LP accelerator with a high quality electron beam combined with an undulator of suitable length. Such an XFEL with a total length of less than 30 m [173], powered by an optical laser, can fit, for example, in a university laboratory and become an excellent compact alternative to current multi-kilometer XFELs such as the LCLS or European XFEL.

The main obstacle to the use of the LP accelerator in a free-electron laser so far has been the insufficiently high quality of the electron beam, in particular, the large transverse emittances [174] of electron beams obtained by the LWFA method. However, ways to overcome this difficulty were shown theoretically in [174]. The Horizon 2020 EuPRAXIA project, part of the European Union's Horizons 2020 innovation research program, was launched in November 2015 with the main goal to develop a technological project for the European Research Plasma Accelerator and its Best Applications [118]. As a result of the implementation of this project, a conceptual report on the design of a compact and cost-effective European physical installation, the world's first high-energy LP accelerator that can provide high-quality electron beams with an energy of tens or hundreds of GeVs, and substantiation of the scope of its applications are scheduled to be issued in October 2019. Actually, as part of the project, the LWFA plasma acceleration method has been optimized and improved to produce electron beams that are suitable for the efficient implementation of laser radiation using the SASE FEL mechanism.

This project was financed from the European Union's Horizon 2020 innovation and research program under grant no. 653782. Funding in the amount of 3 million euros was provided to 16 laboratories and universities from five EU member states under the European Union's Horizons 2020 program [118]. They were joined by more than 20 interested associate participants who make additional contributions to the project. The researchers who have developed and are implementing this program hope to successfully prepare the EuPRAXIA design project and submit it to obtain financing for its technological implementation from the European Strategy Forum on Research Infrastructures (ESFRI) in 2020. This is another important step on the way from the proof-of-concept experiments to real super-compact accelerators for the frontiers of science, industry, medicine, and the power generation industry.

4. Reflective optics for transportation of X-ray beams

The development of X-ray sources, both traditional and alternative, was most strongly influenced by the emergence of new reflective X-ray optical instruments at the turn of the millennium.

Producing many photons for the X-ray probe, i.e., obtaining the maximum intensity of the primary X-ray beam is a very important task of X-ray technology, but it is equally important to deliver these rays to the target without losses. This task should be performed by an X-ray optical system of a diffractometer or spectrometer. For a long time, there were no optical units on X-ray diffractometers except collimating slits and a diffraction single-crystal monochromator, which only greatly reduced the intensity of the radiation generated in XRTs [17, 49, 175]. With the advent in the 1980s of the 'synchrotron radiation era', X-ray mirrors of total external reflection began to be widely used in SR diffractometric stations in addition to slit optical units for collimating and filtering radiation beams [34–36, 81]. However, the mirrors were too long and could not be used in laboratory diffractometers.

The situation changed dramatically at the very end of the 20th century with the creation of technologies for manufacturing highly efficient X-ray reflectors based on multilayer thin-film structures (MTFSs) [21, 24, 25, 176, 177, 186] and capillary glass optics [23, 31, 178–185]. Despite their small size, these X-ray optical elements were able to collect diverging X-rays within fairly wide solid angles, concentrate them, and transmit X-ray photons virtually without loss over long distances.

Reflective X-ray optical elements in the form of thin-film multilayer collimating and focusing reflectors of various shapes, as well as glass capillary optical units, have recently been incorporated in commercially manufactured X-ray sources [75, 175, 184, 187] and are now embedded in diffractometers [31, 188], spectrometers, and other X-ray installations, where they facilitate obtaining unusually bright X-ray beams from laboratory XRTs and various microfocus X-ray sources. Today, industrially produced X-ray optical elements are capable of forming bright X-ray beams that are parallel, diverge at a certain angle, or focus in 2D and 3D dimensions and are applicable in various X-ray diffraction and radiography setups.

4.1 Physical principles of reflective X-ray optics

MTFS-based reflective X-ray optical units and monocapillary and polycapillary reflective optical units essentially use the same phenomenon characteristic of X-rays: the effect of external reflection. All three areas of X-ray optics started being actively developed in the 1980s to attain the level of industrial products in the late 20th and early 21st centuries. Monocapillary collimators and polycapillary lenses exploit the effect of total external reflection (TER), i.e., completely transmit X-rays incident on the inner surface of the capillary at a glancing angle smaller than the critical TER angle ($\theta \leqslant \theta_c$) (Fig. 15), as in the case of X-ray mirrors (see, e.g., [72] or Sections 6.8–6.10 in [34–36]).

These X-ray optical units are achromatic X-ray waveguides, which means that they completely transmit the entire spectrum with wavelengths λ for which the condition $\theta \leqslant \theta_c$ is satisfied, where

$$\theta_c \approx 0.092\lambda\sqrt{\rho}\,. \qquad (5)$$

Here, θ is expressed in degrees, λ in Å, and ρ in g cm^{-3}.

The effect of TER is used in MTFS-based X-ray reflectors [186], multilayer X-ray mirrors, in combination with the interference of X-rays reflected from various layers of the structure. Unlike monocapillary and polycapillary X-ray waveguides, these are monochromatic optical elements that transmit X-rays with a certain wavelength that depends on the glancing angle and MTFS parameters.

4.2 Multilayer thin-film X-ray reflectors

The technology of manufacturing MTFSs developed in the 1980s made it possible to create multilayer X-ray reflectors with a reflection coefficient almost equal to unity, as in TER mirrors, but with a reflection angle tens of times larger than that of a single-layer mirror. MTFSs are made by magnetron depositing of alternating nanometer-thick amorphous layers of materials with very different atomic masses (for more details, see Section 3.3.4 in [34–36]).

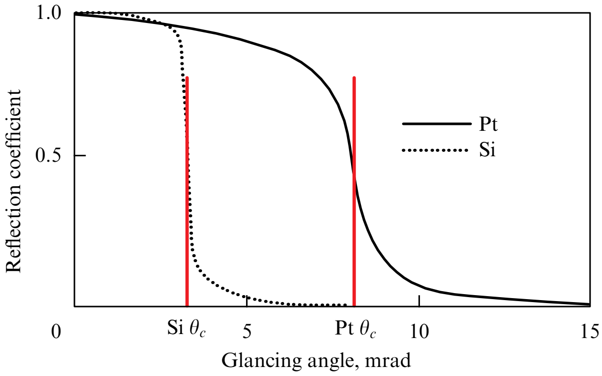

Figure 15. Reflective capacity of X-ray mirrors made of materials with different densities (silicon and platinum) as a function of the glancing angle of X-rays (10 keV radiation, $\lambda \approx 1.24$ Å). (Data are taken from [189].)

The simplest MTFS, schematically depicted in Fig. 16, is characterized by an identity period d, which most often falls in the range 2–6 nm and is manufactured with an accuracy of no less than 1%. Usually, layers of heavy elements (W, Ni, Mo...) are used in X-ray reflectors, and light elements or their compounds (C, Si, B_4C...) are employed as separation layers. These reflectors operate with the X-ray glancing angles θ that substantially exceed θ_c, the critical TER angle (up to several degrees), and therefore they are ten times shorter than flat single-layer X-ray mirrors.

The principle of operation of the MTFS-based X-ray reflector (see Fig. 16) consists in combining the effect of specular external reflection of X-rays and interference amplification of waves from sequential reflecting layers of a thin-film structure. Figure 15 shows that the coefficient of mirror reflection of X-rays from smooth surfaces at glancing angles $\theta > \theta_c$ decreases sharply but does not vanish, even at angles of several degrees (the coefficient remains significant, of the order of 10^{-3} to 10^{-4}). Due to their multilayered structure (usually about 100 pairs of layers) and periodicity, if the Bragg condition $n\lambda = 2d\sin\theta$ is satisfied, MTFSs

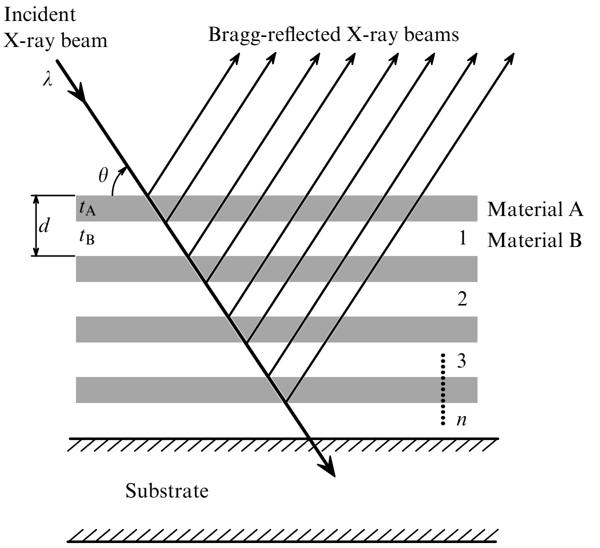

Figure 16. Schematic representation of X-ray reflection from a multilayer thin-film structure with an identity period d.

enable significant (in proportion to the number of pairs of layers squared) enhancement of the intensity of weak reflections as a result of constructive interference. The MTFS operates in this case as a crystal monochromator, amplifying only a narrow (quasimonochromatic) band from the spectrum of incident X-rays, the wavelength of which is determined by the identity period d of the structure and the angle θ that satisfies the Bragg condition.

If the number of pairs of layers in the reflector is sufficiently large, the reflection coefficient of rays with the selected wavelength can ideally be almost 100%, although in practice it rarely reaches 90% due to imperfections of interlayer boundaries and absorption of X-rays in the structure (see [34–36], Section 3.3.4.1). Flat MTFSs are apparently X-ray monochromators with an efficiency close to units (see examples in Section 6.10 of [34–36]), unlike a single-layer TER mirror, which is an achromatic reflector, i.e., reflects the entire spectrum of the radiation incident on it.

MTFSs can be fabricated so as to have a certain curved shape and a period d that varies along the length of the structure (Fig. 17). Such MTFSs with a period varying over length (see [21, 190, 191]) are referred to Göbel X-ray mirrors. The Göbel mirror operates as a focusing Bragg reflector [21]. Owing to its wide aperture, it collects a large number of photons diverging from the X-ray source, selects photons with the energy corresponding to their reflection angle and structure parameters according to the Bragg condition, and redirects them to the sample as a focused or collimated beam (see Fig. 17).

The reflection coefficient of such structures can be tens of percent higher than that of focusing single-crystal monochromators, and the input aperture is several times wider, which allows MTFSs to be used to obtain a significantly larger number of monochromatic photons in a collimated beam.

An ordinary Göbel mirror (see Fig. 17) was originally intended to collimate an X-ray beam in only one direction. To focus X-rays in two directions, two Göbel mirrors mounted perpendicular to each other have been proposed, as shown in Fig. 18. Such reflectors are often referred to as Montel multilayer mirrors. X-ray optical elements of this type were developed by Osmic (USA) under the brand name Confocal Max-Flux$^{\text{TM}}$ [192], and, since the early 2000s, they are mass-produced and distributed, for example, by Rigaku Innovative Technologies, USA [25] (see https://www.rigakuoptics.eom/multilayers/#ovonyx). Göbel reflectors and their combinations in the Montel geometry are also manufactured by Germany-based Incoatec in cooperation with the Bruker AXS company (Germany) of the Bruker corporation [193].

State-of-the-art technologies for the production of MTFSs enable deposition of structures with a longitudinal gradient of the thickness of pairs of layers on substrates curved in a special way (Fig. 19) and thus allow producing two-dimensional and three-dimensional collimators. For example, France-based Xenocs [176] produces and supplies toroidal MTFS reflectors of its own design under the brand name Xenocs FOX3D.

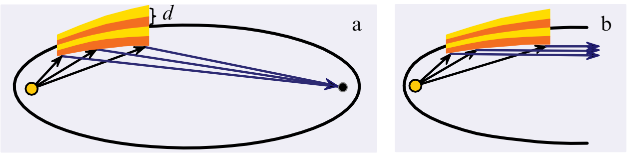

Figure 17. Principle of the Göbel mirror (MTFS with a variable identity period d). The setup of focusing and collimation of an X-ray beam from a point or microfocus source with the (a) elliptical or (b) parabolic shape by multilayer thin-film structures with a gradient of the thickness d of pairs of layers along the length.

The single-reflection MTFS optical elements [26, 176] shown in Fig. 19 provide a more uniform reflected beam than double reflection systems with Montel mirrors (see Fig. 18). If multilayer deposition on a complex-shaped substrate is performed in an appropriate way, the active region of the mirror increases to half the rotation ellipsoid, as a result of which the solid angle of radiation collection increases to 10^{-3} sr (a cone with the angle $\approx 1.8°$).

Parabolic Göbel mirrors have lately been actively used in X-ray diffractometers to form bright beams of parallel rays that are necessary for studying surfaces and thin films by the glancing-beam diffractometry method (see, e.g., [194]) and in a number of other diffraction measurements carried out using the parallel-beam geometry [26]. For example, due to the use of a parabolic multilayer reflector, it is now possible to significantly enhance the characteristics and reduce the dimensions of X-ray diffractometers intended for measurements by the method of small-angle X-ray scattering (SAXS) [25, 193, 195].

4.3 X-ray capillary optics

Glass capillary tubes that can be fully integrated into laboratory X-ray diffractometers proved to be a remarkable and rather inexpensive alternative to flat X-ray mirrors. The principle of transporting X-ray beams through thin glass tubes by means of reflection from smooth inner walls was tested in practice a long time ago [139]. This principle is schematically depicted in Fig. 20.

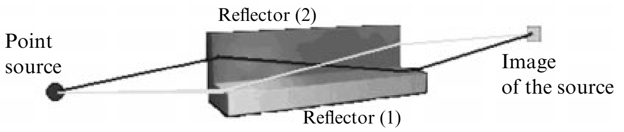

Figure 18. Montel mirror. A setup of the two-dimensional focusing optical element Confocal Max-Flux$^{\text{TM}}$ consisting of two crossed MTFSs with gradients of the period along the length of the structures [192].

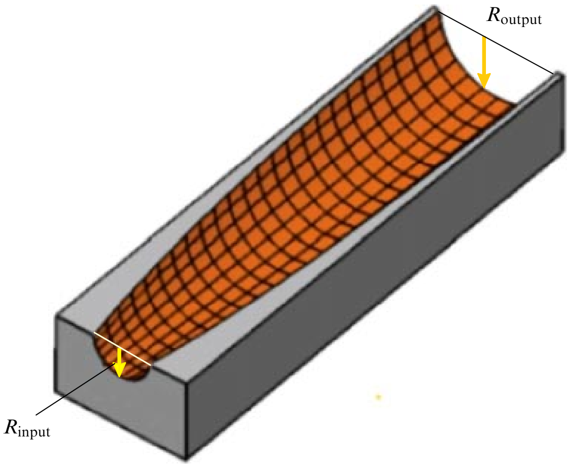

Figure 19. Schematic image of the multilayer thin-film mirror FOX3D CU 14_39 in the form of an ellipsoid of revolution manufactured by Xenocs [176].

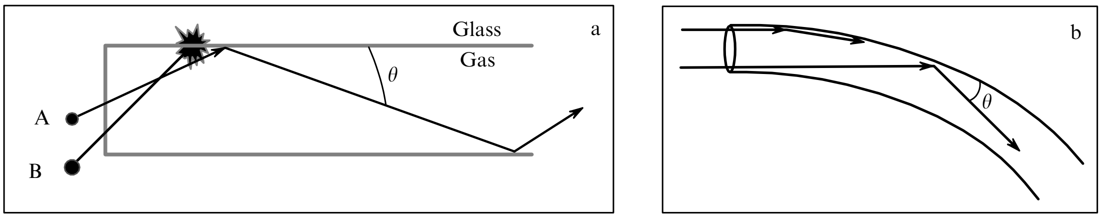

Figure 20. Transportation of X-rays through a glass X-ray waveguide by means of mirror reflection from the walls of the capillary. (a) Beam A, which enters the tube at an angle $\theta \leqslant \theta_c$, experiences total reflection from the walls and propagates along the cylindrical tube without absorption, being then reflected from its inner surface. Beam B, which enters at an angle $\theta > \theta_c$, cannot be reflected, and it therefore penetrates the wall of the tube and is absorbed in it. It follows from the diagram that without absorption, all beams contained within the opening angle $2\theta_c$ propagate through this tube. (b) The path of beams that satisfy the condition $\theta \leqslant \theta_c$ in a curved X-ray waveguide.

Any X-ray incident on a glass tube (Fig. 20a) at a glancing angle less than the critical TER angle is reflected many times from smooth internal surfaces without loss of intensity. In this way, it is possible to transmit the radiation beam over a distance of tens of centimeters, to concentrate the beam of rays, reducing its cross section by means of gradual narrowing of the tube, or to change the direction of its propagation by smooth bending of the channel (Fig. 20b).

Experiments in [139] were performed with soft X-rays with an energy of 1 keV that have a rather large critical angle of reflection from glass ($\theta_c \approx 1.5°$). X-rays from an LP radiation source were transmitted in these experiments (performed as early as the very beginning of the 1970s) through a tube with a channel 8 mm in diameter to a distance of up to 163 cm.

Later, in 1976, the authors of [196] experimentally tested the possibility of transporting harder X-rays (with energies of 5.9 and 14.4 keV, gamma radiation lines of the ^{55}Fe isotope) over long distances via tubular X-ray waveguides with bends. They used a ring assembly of straight and curved glass tubes with an inner diameter of ~ 9 mm along which X-rays were transmitted a distance of 7.3 m. The measured efficiency of transporting photons with an energy of 14.4 keV was about 80% in that experiment. Losses were mainly related to photoelectric absorption in the glass due to the roughness of the channel surface. For more than 10 years after that, there was no noticeable interest in the transportation of X-rays via glass tubes.

Interest in glass X-ray capillary optics rekindled in the second half of the 1980s, and capillary optics developed in two parallel directions: polycapillary lenses [22, 178, 180, 184, 185, 188, 197, 198] and monocapillary collimators [23, 183, 199–201].

4.3.1 Polycapillary X-ray lenses. The forgotten and resurfaced idea of using glass capillaries as X-ray waveguides to channel X-ray photons, to divert their beams at significant angles by means of multiple successive mirror reflections from the walls of a smoothly curved glass tube, and even to compress the beam if it channels along a gradually narrowing capillary was re-examined experimentally and theoretically.[2] New physical calculations in [202, 203] confirmed the possibility of transporting X-rays along a glass tube with a curvature of up to several dozen degrees ($10° - 30°$) with a transmittance of several dozen percent (Fig. 20b). This was the basis on which the idea was formulated in [202] to create X-ray lenses from bundles of glass capillaries bent in a particular way. Next, Kumakhov and co-workers developed a technology for manufacturing glass monolithic blocks that consist of a dense bundle of capillaries with a channel diameter of the order of a micrometer or several dozen micrometers [22, 180] and launched the production of polycapillary X-ray lenses, sometimes referred to as Kumakhov lenses. The principle of operation of Kumakhov lenses is shown in Fig. 21. Depending on the purpose (collimation or focusing of the beams), capillaries in the block are produced with a certain curvature and a variable cross section that determine focal lengths. A bundle consisting of many capillaries can efficiently capture and shape an X-ray beam.

Such lenses, which are now commercially manufactured, are widely used in X-ray technology to focus, shape, and collimate X-ray beams [178, 185, 188, 198, 204]; presently, any X-ray diffractometers can be optionally equipped with them at the user's request. Due to the exceptionally wide angle Φ of the capture of radiation, polycapillary lenses are especially effective if working in combination with microfocus XRTs. Kumakhov lenses made it possible to significantly expand the capabilities of X-ray diffractometers. Their characteristic feature is a very large angle Φ (see Fig. 21) in which radiation from the source is captured ($5° - 10°$, depending on energy); as a result of this [31, 178, 184, 188], the Kumakhov lens enhances the photon flux density by several orders of magnitude in an area close to its focal point.

Such lenses enabled diffraction imaging using a microfocus tube with a power of the order of 1 W, which is as efficient as using a fine-focus tube for structural analysis with a power of the order of 1 kW but without the focusing polycapillary optical elements [188]. Polycapillary half-lens units (Fig. 21b) also provide a sufficiently wide and intense beam of parallel X-rays from a microfocus XRT or from an LP source, a feature that is of importance for diffraction measurements in the Debye–Scherrer geometry or for small-angle X-ray scattering (SAXS). Moreover, focusing capillary optical elements, like X-ray mirrors in experimental stations on SR channels [34–36], effectively suppress the hard part of the X-ray spectrum, for which the critical angles of glancing reflection are much smaller than for rays in the soft region of the spectrum.

Modern polycapillary lenses of the latest generation with submicron channels have a length of only about 1 cm, and can

---

[2] The most amazing aspect of this situation is that researchers (and not only Russian ones) re-addressed the problem of X-ray transportation along glass tubes, including bent ones, from scratch, as if there had been no publications in renowned international physical journals (*Appl. Phys. Lett., J. Appl. Phys., J. Opt. Soc. Am.*) where the possibility of turning X-rays by large angles and transporting them over long distances with very small losses of intensity had been experimentally and theoretically confirmed a decade earlier.

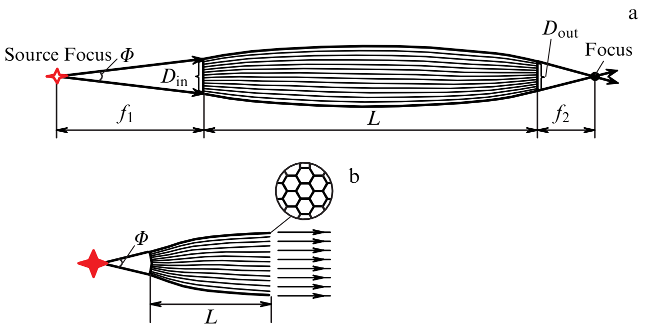

Figure 21. Operation of (a) polycapillary focusing and (b) collimating X-ray lenses (Kumakhov lens and half-lens). The lenses are characterized by the optical length L, the entrance focal length f_1, the exit focal length f_2 (for a focusing lens), diameters of the entrance and exit apertures D_{in} and D_{out}, and the angle of capture Φ. The focusing lens (a) captures X-rays from the source within the angle Φ and focuses them onto a spot located at a distance f_2 from the exit end of the lens. A collimating lens (sometimes referred to as a Kumakhov 'half-lens') also captures a beam of rays diverging from the source and gathers them into a beam of parallel rays. The half-lens can be used in the reverse direction and focuses parallel beams (for example, synchrotron radiation) on a micrometer-sized spot of extremely high brightness. A cross-sectional view of a part of the polycapillary optical device is schematically depicted in the circular inset in figure (b).

be easily integrated into any X-ray diffractometer in place of a regular primary beam collimator. Kumakhov lenses today have the largest reception aperture (i.e., capture angle) among all X-ray optical elements, including MTFS and glancing reflection mirrors. This enables their successful use in combination with regular XRTs to obtain radiation beams of enhanced brightness or the development of a 'virtual' radiation source with a given shape of the focus, for example, linear or point-like. Studies conducted by Bruker AXS showed that if a polycapillary lens with a microfocus XRT (Mo anode) is used, the brightness in a focal spot about 25 μm in diameter is ten thousand times higher than that obtained at the same place from the same source if a regular tubular collimator is employed (see https://www.bmker.com/en/products/x-ray-diffraction-and-elemental-analysis/micro-xrf-and-txrf/m4-tornado/technical-details/spot-size.html).

4.3.2 Monocapillary collimators. Monocapillary X-ray optical elements were developed concurrently with Kumakhov's polycapillary optical units [23, 183, 200, 201]. This X-ray optical element is attractive because it provides a brightness enhancement effect, while being externally and functionally very similar to standard slit or tube collimators routinely used in the X-ray techniques. The most common setups of monocapillary collimators are presented in Fig. 22, where Fig. 22a shows a simple cylindrical collimator in the form of a smooth glass tube.

A cylindrical glass capillary is actually an analog of a single channel of a polycapillary lens. Because the TER effect collects all the photons entering within the cone (Fig. 22a) with an opening angle of $2\theta_c$, even such a simple collimator yields an increase in output brightness compared to a similar tube collimator without the TER effect, as was reported in [139].

To increase the output radiation brightness even more, the angle of capture of diverging rays at the collimator input is increased, and the rays are focused at the output by shaping the capillary in the form of an ellipsoid or a paraboloid [23, 200, 205, 206], as shown in the diagrams in Figs 22b–g.

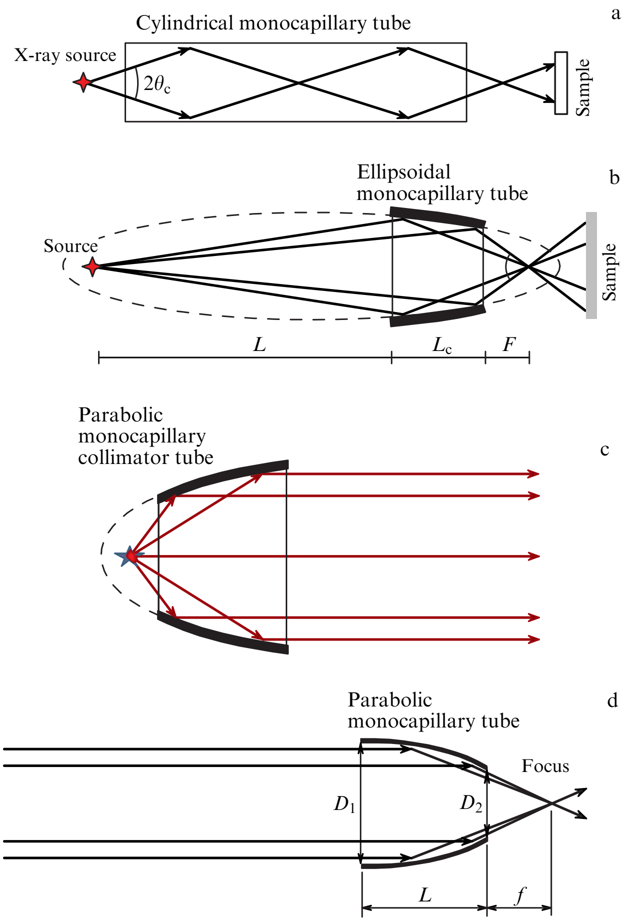

Figure 22. Principle of operation of monocapillary glass mirror-reflection collimators. For clarity, the angles in the figures are greatly exaggerated. The critical angles of mirror reflection of X-rays are usually $\theta_c < 0.5°$; therefore, the angle of capture of radiation by the monocapillary collimator is noticeably less than 1°. (a) A cylindrical collimator (X-ray waveguide), (b) an elliptical focusing monocapillary single-reflection collimator, (c) a parabolic monocapillary single-reflection collimator in the geometry of diverging X-ray beam conversion to a parallel beam (the point source should be located at the focus of the parabola), (d) a parabolic monocapillary in a device that microfocuses a beam of parallel X-rays.

A monocapillary collimator consisting only of a single hollow glass tube of a certain shape can focus X-rays onto a spot of a micrometer or even sub-micrometer diameter, no worse than a polycapillary lens does. Moreover, the ellipsoidal monocapillary collimator with single mirror reflection (single bounce collimator, SBC) in Fig. 22b can increase the flux density of photons in the beam by a factor of hundreds (10–500), although the angle of capture of rays from the source is < 1° for this collimator, a value that is not as large as that of polycapillary lenses [183].

Elliptical monocapillary single-reflection collimators (Fig. 22b) can have a large focal length F (up to tens of centimeters [183]), as a result of which they can be easily used in ordinary single-crystal and powder X-ray diffractometers. Due to the large distance between the end of the collimator and the sample, the maximum available diffraction angle is increased, thus providing the necessary operational free space around the sample on the goniometer. The sample under study is usually placed at a distance equal to 10–100 diameters of the collimator output hole to locate it behind the focal point in a sufficiently wide beam [23].

The parabolic X-ray monocapillary collimator is actually an optical projection single-reflection system. It can be used either to focus a beam of parallel X-rays onto a small-size spot (Fig. 22d) or, if used in the inverse direction (Fig. 22c), to transform X-rays diverging from a point focus onto a parallel beam.

The transmittance capacity of glass monocapillary collimators and X-ray waveguides is close to 100%, i.e., they transmit virtually all the photons that they capture. As a result, more than one such optical element of various types can be used with an insignificant loss of intensity to obtain an X-ray beam with the required geometric characteristics [23]. For example, to obtain a beam of parallel rays using the parabolic collimator in the setup shown in Fig. 22c as a point source, beams diverging from the focus of an elliptic collimator can be used (Fig. 22b).

X-rays focused using SBC collimators can be used in a variety of experiments. For microscopic X-ray imaging of microbeams, the sample should be placed at the focal point *f*. In actual macroscopic diffraction measurements, the sample is placed behind the focal point (if measuring from the collimator end) to ensure that the exposed area of the sample is not too small and, in the case of single-crystal X-ray diffractometry, to ensure the condition of the crystal 'awash with ray beams'. For this, the sample is placed at a distance of several centimeters behind the focus, where the beam diameter is larger than a micrometer or sub-micrometer-sized focus, and the rays are gathered into a slightly diverging beam.

5. Next-generation X-ray sources based on X-ray tubes

New sources of X-rays are developed in many ways. It should be admitted, however, that so far no alternative sources of X-ray radiation are as widely used as XRTs and SR sources. The number of published applications of these alternative sources for XRD studies is still negligible compared to the number of applications of XRTs or SR. However, even in the case of SR sources, despite the excellent characteristics of their radiation, users encounter serious problems related to the small number of these sources and to access to these sources for operational research in science, industry. and medicine. Third- and fourth-generation SR sources are giant resource-sharing facilities, whose construction and operation require multimillion-dollar investments and can only be done by governments or major corporations.

The much smaller alternative X-ray sources discussed above can be developed and produced even by small companies and used by individual laboratories at their discretion for any operational research. However, such sources have not yet become widespread commercial products, either due to unresolved technological problems or because of their insufficient efficiency compared to the costs of their manufacture and maintenance. It is for this reason that, to meet the needs of numerous users of X-ray devices and facilities, improvement in XRT-based sources of X-rays is in progress.

The development of new types of XRTs, despite the crisis of their development that emerged at the end of the 1980s [186], did not halt and continues to date; at the beginning of the 21st century, they were moved up to a qualitatively new level and became quite successful and promising. This progress was catalyzed by the spectacular achievements discussed above in the development of reflective X-ray optical units and X-ray transport channels at the end of the 20th century, which enabled the renaissance of XRTs in the 21st century.

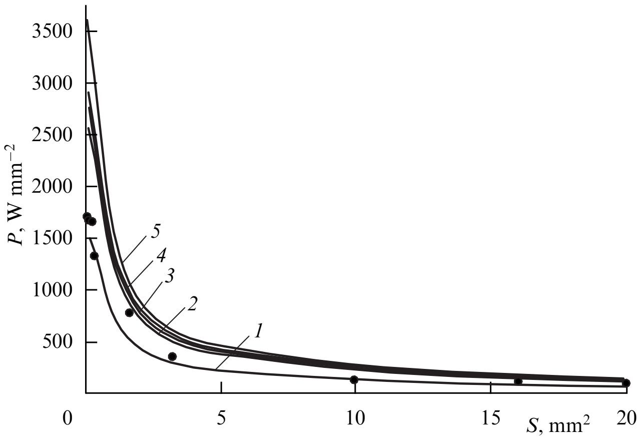

Figure 23. Maximum allowable surface power density of the fixed anode of an XRT with a normal focus as a function of the cross-sectional area of the electron beam. Silicon anode of various thicknesses: 1 mm (*1*), 0.5 mm (*2*), 0.25 mm (*3*), and 0.1 mm (*4*). Tungsten anode 0.5 mm thick (*5*). Dots indicate experimental data. (Plot is taken from [208].)

Achievements in the development of laboratory XRT-based X-ray sources at the beginning of the 21st century are associated with a change in strategy in the design and manufacture of X-ray sources — the transition from XRTs of large (multi-watt) electric power and emitting-region dimensions (XRT focus) of the order of several square millimeters to microfocus XRTs with a focal diameter of less than 50 μm and a power of less than 50 watts, combined with highly efficient collimating and focusing X-ray optical elements. It became possible as a result to significantly increase the brightness of the XRTs and to dramatically reduce the loss of X-ray photons produced by the source.

Theoretical and experimental estimates in [186, 207, 208] of the maximum power density of the anode current at which an XRT is able to operate without rapid destruction of the anode due to overheating found a trend that this limit increases as the focus size decreases (Fig. 23).

Studies [186, 209] showed that heat removal from the electron beam absorption region in the anode is significantly enhanced if the beam diameter is less than 100 μm (usually 50 μm or less), to the extent that in a microfocus XRT, without melting the anode, it is possible to achieve anode current power densities that are tens or even hundreds of times greater than those with a millimeter-size electron beam in XRTs with a stationary or rotating anode (Fig. 24).

5.1 Microfocus X-ray tubes with a stationary anode

Microfocus tubes appeared in X-ray diffractometry at the very end of the 20th century and early in the 21st century; they consumed electric power tenths or even hundredths that of fine-focus XRTs or X-ray generators with a rotating anode, which were used earlier in X-ray diffractometers. It turned out that low-power microfocus tubes are very efficient sources of X-rays if combined with high-quality state-of-the art focusing reflectors and X-ray collimators that have a large angle of capture of the X-rays leaving the

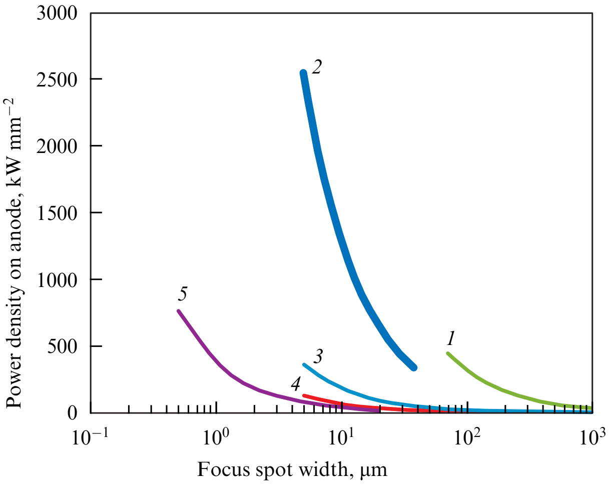

Figure 24. Maximum current power density of an electronic XR beam as a function of the focus spot size on anodes of various types. (*1*) Rotating anode (1:10 linear focus), (*2*) Liquid-metal-jet anode (1:4 linear focus), (*3*) Stationary solid target (1:10 linear focus), (*4*) Thick solid target (round microfocus), and (*5*) Transmission target. (Plots are taken from [209].)

XRT focus and can focus and transport these rays without loss. They can deliver X-ray beams to the sample for diffraction measurements with an intensity that is not less than that of beams from the most powerful XRTs with a rotating anode and macroscopic focus, but with an energy consumption that is thousandths as high!

These ‘low-power’ X-ray sources only appeared at the forefront due to the emergence of reflective monocapillary and polycapillary optical devices and collimating multilayer thin-film mirrors. Without these small accessories, microfocus XRTs were for a long time of no interest due to the small dimensions of the source and smallness of the integral photon flux in the corresponding beam of parallel rays provided by the microscopic focus.

Microfocus XRTs used for X-ray diffractometry that are currently available on the market are all structured in approximately the same way and have similar technological characteristics [177, 187, 204, 210]. Most often, they are designed as tubes with a thick anode and one side window through which a finely focused electron beam about 10 μm in diameter, which delivers electric power of the order of 30–50 W, irradiates a spot 20–50 μm in diameter on the anode plane, which is tilted to the beam (Fig. 25a). The electrical load density on the anode can be as high as 100 kW mm^{-2}, a value that is approximately 120 times the specific load density on the anode of a regular sealed tube with a power of 2.5–3.0 kW and almost 10 times more than that of regular rotating-anode tubes with a power of 5–15 kW.

Due to the small size of the region heated by the electron beam a micrometer in diameter and the dissipation of heat from it in all three dimensions, the anode in the microfocus XRT does not melt and operates in a stationary thermal mode under cooling with flowing water typically used in XRTs and even under air cooling.

Figure 25a shows how a beam of parallel X-rays with a cross section equal to the visible size of the XRT focus is separated from a microfocus using a regular tubular collimator (aperture diaphragm). All radiation outside the collimator hole is absorbed by the aperture slit. This setup has been used for many decades in X-ray diffractometry. To obtain a high-flux photon beam in next-generation diffractometers, rays are collected and collimated from a wide solid angle (from several degrees to tens of degrees) using either a polycapillary lens or an ellipsoidal MTFS-based 3D reflector [176] (see Fig. 19). In testing [176] a 50 W microfocus XRT with a copper anode in combination with a reflector of this type, a flux onto an 80×80 μm spot as high as 4×10^8 photons s^{-1} was obtained, while if a tubular collimator without a reflector was used, the flux in the same spot was only 2.6×10^7 photons s^{-1}. Thus, the ellipsoidal parabolic reflector collimator FOX3D Ci 21-21HC (Xenocs) boosted the intensity of the monochromatic characteristic radiation of Cu K$\alpha_{1,2}$ by more than ten times due to the collection of diverging rays from a cone with an angle of $\approx 1.8°$ and compression of those rays into a narrow beam. This value is almost 100 times greater than that obtained when using a tubular collimator from a regular sealed fine focus XRT with a power of about 1.5 kW.

Figure 25b schematically depicts a polycapillary half-lens that collects the X-rays emerging from a microfocus ~ 50 μm in diameter into some solid angle and forms a parallel beam from these rays [211]. Owing to the collecting lens, even with a microfocus XRT with a power of only about 30 W (current of about 800 μA), the integral photon flux in the area of the sample under study was higher than that from a regular fine focus sealed tube for XRD with a power of 2.5–3.0 kW

The brightness of microfocus sources that consist of tubes of this design combined with reflective polycapillary collimating optics is two orders of magnitude higher than that of sealed XRTs for XRD [204] and exceeds the brightness of rotating-anode tubes by more than an order of magnitude. The point is that the X-rays emerging from the microscopic

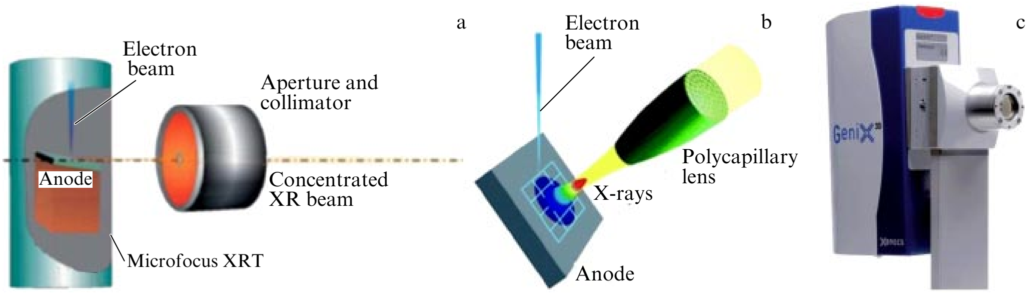

Figure 25. Setup and principle of operation of a state-of-the-art X-ray source with a microfocus XRT and reflective X-ray collimating optical element. (a) Setup with a tubular collimator, (b) setup with a polycapillary collimating lens, and (c) photographic image of the GeniX 3D microfocus tube unit combined with the FOX3D MTFS reflector (see Fig. 19).

focus of the tube within a cone with an angle of about 20° can be fully captured, for example, by polycapillary glass half-lenses, as is shown in Fig. 25, almost completely transformed into a concentrated collimated or focused beam, and delivered without losses to the sample under study. Nearly the same can be achieved by means of state-of-the-art focusing thin-film multilayer reflectors.

The idea, suggested by Arndt [186], to combine microfocus tubes with X-ray optical collimators consisting of polycapillary half-lenses or Kumakhov lenses or with focusing MTFS reflectors into a single unit directly at the factory (Fig. 25c) and to supply such a combined source of assembled radiation proved to be very fruitful, and it is now being implemented and developed by manufacturers and suppliers of microfocus XRTs [177, 187, 204], such as Incoatec (Germany) (in cooperation with Bruker AXS), PANalytical (UK) (in cooperation with Rigaku), and Xenocs (in cooperation with MAR Research, USA). This design is attractive because, while ensuring a very good brightness, it does not require any maintenance, does not need to have collimators and monochromators adjusted, consumes very little electricity and energy for cooling, and is very compact. At present, microfocus X-ray sources are commercially manufactured with both water cooling, for example, metal-ceramic 30-W MCBM 50–0.6 B microfocus tubes (XRW — Röntgen-Technik Dr. Warrikhoff GmbH & Co. KG) and with air cooling, for example, IμS (Incoatec) tubes with the same power that is widely used in diffractometers manufactured by Bruker AXS. X-ray diffractometers with such X-ray sources have recently become very popular [31, 177, 188, 193, 210, 212] in single-crystal and powder X-ray analysis and in SAXS methods.

5.2 Microfocus X-ray tubes with a liquid-metal-jet anode

An original solution to further increase the brightness of the microfocus XRT was found by engineers at Sweden-based Excillum [76, 213, 214], who abandoned struggling with the anode melting but used a thin stream of already molten metal as the anode. In the XRT that they proposed, a liquid Ga–In alloy with 95% gallium at a temperature slightly above 50 °C is pumped along a closed circuit and bombarded by a focused intense electron beam to produce a very bright X-ray beam at a Ga Kα wavelength of 1.34 Å (photon energy 9.25 keV). Unexposed liquid target material is supplied by the compressor at a rate of about 50 m s^{-1} and the anode load, which can be $>$ 1000 kW mm^{-2} and is only limited by the onset of intense evaporation of the melt, which, according to estimates [213], should be observed at a power density of about 12 MW mm^{-2}.

Based on this idea, Excillum (Sweden), in collaboration with Bruker Corporation, designed a commercial version of the METALJET microfocus X-ray source [31, 209, 215], which Bruker AXS has been installing since 2014 in some D8 VENTURE single-crystal X-ray diffractometers for protein research (Fig. 26a). At the same time, the Bruker AXS uses its proprietary multilayer HELIOS MX thin-film reflector (Göbel mirrors in the Montel geometry) in the source for the selection, monochromatization, and transportation of the X-ray beam. The photon flux density in the radiation beam of this new source, which is of the order of 10^{11} photons^{-1} mm^{-2}, exceeds the brightness of the most powerful X-ray generators with a rotating anode available today (see Fig. 5).

Incoatec and Bruker AXS specialists note in [216], however, that to ensure the reliable operation and extreme brightness characteristics of the METALJET sources, regular maintenance, sometimes for a very long time, is needed.

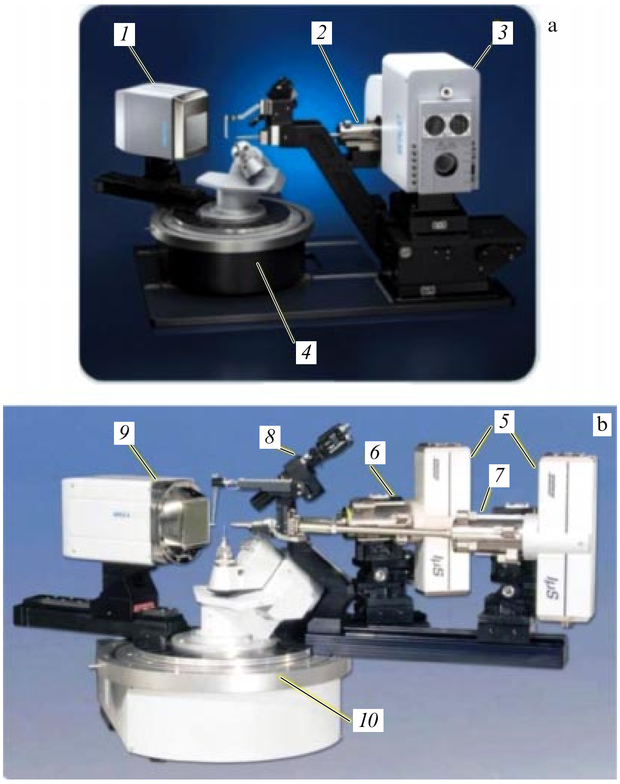

Figure 26. Example of a state-of-the-art X-ray diffractometer with various radiation sources. (a) D8 VENTURE (Bruker) diffractometer with a METALJET X-ray tube with a liquid metal anode: *1* — two-dimensional PHOTON detector, *2* — X-ray optical element, *3* — METALJET X-ray source assembled with focusing reflective optics, *4* — X-ray goniometer. (b) D8 VENTURE diffractometer with two microfocus XRTs: *5* — type 1 and 2 radiation sources (for example, with Cu and Mo anodes), *6*, *7* — reflective X-ray optical elements of sources 1 and 2, *8* — adjustment telescope, *9* — two-dimensional APEX detector II, *10* — X-ray goniometer.

Therefore, if there is no urgent need for the maximum intensity of the primary X-ray beam provided by a radiation source with a liquid metal anode, it is preferable to use sealed microfocus X-ray sources with a fixed anode (Fig. 26b), such as Incoatec Microfocus Source IμS [193] or GeniX 3D manufactured by Xenocs (Fig. 25c), which are much cheaper than METALJET or rotating-anode tubes and do not require any maintenance at all. Such tubes with focusing MTFS reflectors can provide flux densities of the order of 10^{10} photon s^{-1} mm^{-2} in a beam focused on the sample. Due to the small size, two microfocus sources with various wavelengths are often installed on state-of-the-art diffractometers, as shown in Fig. 26b, which can be used alternatively without additional adjustments and settings, even to examine a single sample.

6. New X-ray detectors

Equations (2) and (3) show that the accuracy of XRD measurements and the sensitivity of the experiment depend on the intrinsic background of the detector; in addition, the rate and reliability of the measurements depend on both the detector and the brightness of the source. The high speed of measuring diffraction patterns was in demand in the 1980s with an increase in the amount of research on XRSA of proteins and macromolecular crystals, where a huge number of interference reflections from one crystal had to be measured. To collect immense amounts of data, for example, for the XRD of proteins, 2D position-sensitive detectors of various types commenced to be developed, manufactured, and applied in the 1980s, as were various linear (1D) coordinate-sensitive detectors in powder X-ray diffractometry [28, 29, 31, 34–36, 49, 217–220]. These devices, like a photographic film, simultaneously record X-ray photons in an array of points located in a large area of diffraction space and simultaneously determine the coordinates of these points. Used as such 2D coordinate-sensitive electronic-detection devices were, first, multi-wire gas-filled proportional counters (for example, X-100 manufactured by Siemens/Bruker); solid-state television detectors (for example, Fast manufactured by Enraf-Nonius (Netherlands), see [49, 218, 221]); and electronically readable plates with optical memory (Imaging Plate (IP) detectors) manufactured, for example, by MAR Research and Rigaku (see [219] or Section 3.2 in [34–36]).

From the very moment of their emergence, 2D detectors greatly contributed to the development of XRD and XRSA, significantly changed the procedure for measuring and processing diffraction data, and significantly (by a factor of tens) boosted the speed of experiments, while concurrently expanding the range of objects available for analysis by means of laboratory diffractometers [219, 222–224]. 2D detectors also exhibited high efficiency in the diffractometry of powders [220] and noncrystalline materials [228], providing an increase in the speed of measurements of total scattering diffractograms [18] by a factor of hundreds [225] and enriching the information content of the data set, for example, by detecting texture or sample heterogeneity. They turned out to be incomparably more efficient and more accurate in collecting diffraction data for the structural analysis of conditionally crystalline or noncrystalline samples by using the pair distribution density function (PDF) [3, 18, 226–228] or the Debye function [18, 229].

6.1 Two-dimensional detectors based on charge-coupled devices

Among all the types of 2D X-ray detectors that appeared on the market in the early 1980s, the greatest popularity, owing to the widespread development of macromolecular crystallography on SR sources, was gained by 2D television detectors [230] — electronic detectors with a fluorescent screen that converts X-ray quanta into light flashes transmitted through photo-optical fibers (Fig. 27a) to photodetecting electronic devices. Based on this three-stage technology (fluorescent screen + structured bunch of glass fiber optics + photosensitive matrix to record the optical signal from each fiber) and application of new photodetecting matrix chips (Charge Coupled Devices; CCDs), CCD detectors have been created that feature a fast response and relatively fast reading of the recorded information to the control computer [230]. However, due to the cone-shaped glass fiber optical elements that contract the fluorescence screen image to the size of the detecting chip (Fig. 27c), CCD detectors were too heavy to be used in laboratory X-ray diffractometers. Nevertheless, they were widely and successfully used to measure the structure of macromolecular crystals in SR, where the restrictions on weight and dimensions are not that significant.

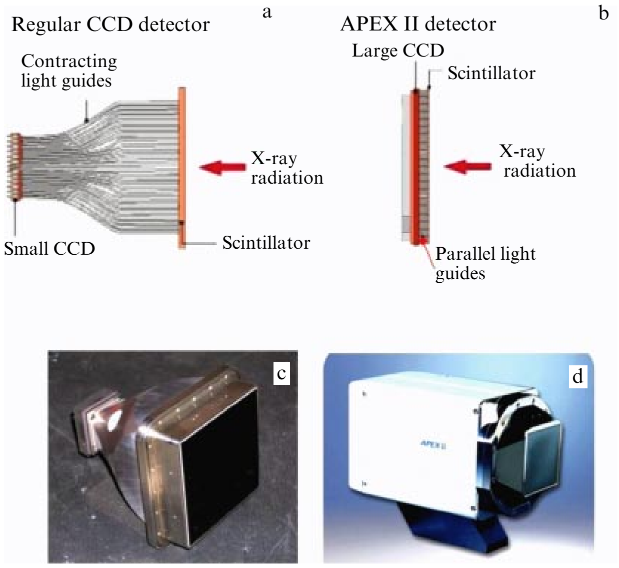

Figure 27. Setup of the device and an exterior view of 2D X-ray coordinate-sensitive CCD detectors. (a) Setup of an old regular CCD detector with a conical light guide, (b) setup of a new CCD detector with a large matrix and straight light guides, (c) view of a regular CCD detector with a conical light guide without a casing (fluorescent screen of the module is usually about 100 mm wide), (d) exterior view of the Bruker APEX II detector (straight light guide, active window area of about 80 × 80 mm).

After their appearance, 2D coordinate-sensitive CCD detectors rather quickly and almost completely monopolized the collection of XRD data from SR sources, where the time factor is of significant importance. For example, by 2006, they accounted for more than 90% of the X-ray detectors used in the beams at ESRF, Europe's largest synchrotron radiation source [222]. The other most common detectors were mainly IP detectors with built-in image scanners.

IP detectors [31, 232, 233] have long been used as 2D coordinate-sensitive detectors in laboratory X-ray diffractometers; while having a wide receiving aperture [231], they are quite light. However, despite the many advantages of IP detectors, their significant drawback has been and remains the long time (from 1.5 to 4 min) needed for the laser scanner to read the measurement results, an operation that is repeated many times during the entire single-crystal imaging cycle, and unavailability of the results of imaging in the course of the experiment.

The CCD detectors [230] that appeared at the turn of the century had no delays in reading information, but the need to use a compressive conical optical fiber (Fig. 27a, c) to couple a wide receiving scintillation screen with a small detecting CCD matrix not only increased the weight of the detector but also greatly reduced sensitivity, because most of the photons from the scintillator (more than 90%) were lost in the optical fiber. Apart from this, all detectors with fiber-optic elements feature a characteristic background noise due to foreign photons of spurious radiation generated in fiberglass on the path between the scintillator and the CCD, which reduces the measurement accuracy. Moreover, in most cases, the matrices themselves have a large dark current (i.e., background) at room temperature, which requires active cooling of these chips to suppress the background [28, 29].

This drawback of radioluminescent detectors has been recently removed to a significant extent by replacing CCD matrices with AP CMOS (active pixel complementary metal oxide semiconductor) integrated pixel matrices [234]. This technology has been implemented, for example, in PHOTON series X-ray detectors (Fig. 26a) manufactured by Bruker AXS.

Given the great number of household appliances such as digital cameras and mobile phones with touch screens produced in the world, launched in the first decade of the 21st century was the manufacture of large-size light-sensitive matrix chips capable of capturing an image of a laboratory 2D detector scintillator with a receiving window of about 80 mm without compression. This progress eventually enabled removing the heavy conical glass light guide from TVs (which provides optical communication between the screen and the CCD matrix) and replacing it with a thin fiber optic lens with a 1:1 magnification (Fig. 27b). This allowed significantly reducing the weight of the detector and enhancing its efficiency by reducing the loss of photons in the optical fiber. For example, the weight of the new Bruker APEX II CCD 2D detector (Figs 26b and 27b, d) with a direct fiber-optic transition from the phosphor to the CCD is approximately one fourth that of the preceding detector with a conical light guide and similar dimensions of the input window.

For example, we compare the main characteristics of two types of television detectors measured by Bruker AXS specialists [235]: the old CCD detector with a conical compressive light guide and the new APEX II detector with a thin direct fiber-optic lens. The transmission capacity of cone-shaped fiber-optical elements in regular-design CCD detectors is less than 10%, while a 1:1 fiber-optic lens transmits more than 70% of the photons from the screen to the CCD matrix. The 1:1 image used in the APEX II CCD detector improves optical transmission by an order of magnitude. The sensitivity of the APEX II detector, according to [235], is 15 times higher than that of the classic CCD detector, as a result of which it can collect diffraction data from microcrystals or very weakly scattering crystals. The main achievement is that the next-generation CCD detector is quite suitable in terms of weight and size for installation on ordinary laboratory X-ray diffractometers, this opportunity being employed in the production and supply of single-crystal diffractometers by a number of companies, such as Bruker AXS.

Common to CCD detectors (see Fig. 27) is the principle of X-ray detection using a luminescent screen, which determines the sensitivity and efficiency of the detectors and which is the root of their shortcomings. Although the sensitivity of phosphor depends on the wavelength, none of the radioluminescent-type detectors provides energy resolution. Moreover, the presence of phosphor limits the possibility of enhancing the spatial resolution of coordinate-sensitive detectors. For example, the pixel sizes of CCD chips in both detectors under consideration are approximately the same and rather small (about 15 μm). However, such a high spatial resolution of the chip does not imply a high resolution of the detector. The signal from an X-ray photon detected in the scintillation screen spreads in width and can be detected by a pixel about 150 μm in size. Thus, despite the high spatial resolution of the CCD matrix, the spatial resolution of the detector is determined by the spread of the signal in the phosphor, which is ten times the CCD-matrix pixel. A major drawback of luminescent-type detectors [230] is the damage to the touch screen made by intense X-rays, for example, the burning out of phosphor by a direct beam from an XRT. Finally, the image can be distorted in both CCD detectors by the detection-system electronics. For example, image quality can degrade due to residual dark current or due to shot noise in the process of reading, as well as due to spreading of the signal in the phosphor and optical elements. CCD detectors have a high level of intrinsic noise at room temperature [222], and therefore require cooling of the CCD chip, often to negative temperatures on the Celsius scale.

The dynamic detection range (the difference between the minimum and maximum possible intensities) of radioluminescent CCD detectors is greatly limited by the presence of a long after-glow effect at the luminescent-screen points [222, 230], where bright reflections are recorded. This effect severely limits the maximum possible frame rate and the speed with which diffraction data are collected. The problem of afterglow is associated with prolonged attenuation of the image after the cause of its occurrence disappears. For example, if images of diffraction patterns are obtained using the single-crystal rotation method, diffraction spots appear, glow, and then disappear. The image on the radioluminescent screen is constantly changing: a strong reflex can be superseded by a weak one by the time the next frame is recorded or nothing may appear at all. However, a high afterglow background remains in this spot, which, if images are taken rapidly, may be mistaken for diffraction reflex. If an intense source of synchrotron radiation is used, the crystal may rotate very rapidly and the time between changing of spots can be a few tenths of a second. Most phosphors fail to dim in such a short time. The narrow dynamic range and low frame rate due to afterglow effects also limit the applicability of CCD detectors for time-resolved experiments, such as studying irreversible phase transitions or measuring characteristics of metastable phases, not to mention faster processes whose lifetime is measured in picoseconds [95].

6.2 Semiconductor position-sensitive detectors

The landscape of the market of X-ray diffractometer detectors changed dramatically at the beginning of the 21st century. Semiconductor pixel (2D mosaic or matrix) [236, 238] and strip 1D detectors [28, 29, 237, 239], which came from elementary particle physics, pushed the CCD and IP detectors to the background by eliminating the shortcomings that became an impediment to further development of X-ray analytical methods. Technologies of detection by direct conversion of absorbed X-ray photons into electrical signals in semiconductors implemented in 1D and 2D coordinate-sensitive detectors [28, 29] have been employed to record X-ray images with SR since the late 1990s. They were rather rapidly incorporated into laboratory X-ray diffractometers with XRTs and greatly changed the methodology of XRD experiments [240–244] and expanded their capabilities [31, 219, 244].

The principles of operations of semiconductor detectors, including position-sensitive matrix detectors, have been known for a long time (for example, the patent [245] for the invention of such a detector was registered as early as 1965), but their practical implementation was hindered by the absence of semiconductor materials with the necessary physical characteristics and insufficient level of development of microelectronic technologies that would enable the manufacture of effective X-ray detectors capable of operating in a stable way under normal conditions without cryogenic cooling. Such materials and technologies appeared by the end of the 1990s [246–248]. Based on these technologies, it finally became possible to develop semiconductor array position-sensitive detectors that significantly boosted the accuracy, operation rate, and efficiency of X-ray research methods [225, 244, 247, 249, 250], and not of diffraction alone, but also of spectroscopic and radiographic techniques.

The basis for state-of-the-art coordinate-sensitive linear (1D) and 2D semiconductor X-ray detectors is the long-known principle of silicon p–i–n photodiodes [251] (Fig. 28a). Owing to the extremely high radiation resistance, X-ray sensitive silicon p–i–n diodes were used in the late 1980s at large SR sources as photon beam detectors/monitors in radiation channels, in addition to ionization chambers commonly used for this purpose [34–36, 252, 253]. These photodiodes, compared with p–n junction semiconductor detectors widely used in elementary particle physics, contain a rather thick layer (from several dozen to hundreds of micrometers) depleted in charge carriers to the level of intrinsic conductivity.

In the case of an Si single crystal, such a material has a specific resistivity up to 4000 Ohm cm and, at a thickness of about 350–500 μm, provides absorption and efficient detection of X-ray photons with energies up to 20–25 keV [246], which are typically used in XRD methods. The basic properties of silicon p–i–n diodes and X-ray detectors based on them can be found in many books and publications (see, e.g., [244, 247, 248] or Section 3.2 of [34–36]). A list of the most attractive properties of these detectors includes a high counting rate, low intrinsic noise [246, 251, 252, 258], extremely high radiation resistance, and fairly good energy resolution that ensures that detectors of this type are undoubtedly superior to all previously used X-ray detectors.

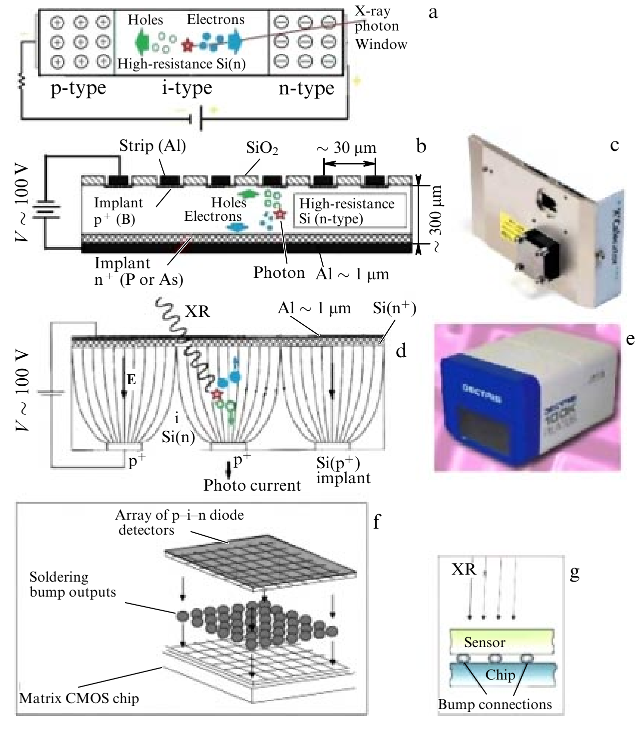

Figure 28. (a, b) Block diagrams of semiconductor X-ray detectors based on high-resistance Si (i indicates n-type conductivity, specific resistance of about 4 kOhm cm): (a) point p–i–n photo diode in the mode of counting quanta, i.e., with inverse offset voltage of carriers applied, (b) strip detector [28, 29, 237, 239] — 1D detector: the strips are usually about 50 μm wide and about 10 mm long, (c) photograph of a 1D X'Celerator strip semiconductor detector developed by PANalytical [239] for X'Pert PRO powder diffractometers (window 9 × 15 mm, active length 9 mm), (d) sensor of a silicon pixel detector (2D detector) [30, 237, 254–256], (e) exterior view of a PILATUS 100K hybrid semiconductor pixel detector manufactured by DECTRIS Ltd. (Switzerland) (active window area of about 83.8 × 33.5 mm), (f) connection circuit of the sensor array elements with the corresponding array elements of the CMOS integrated circuit that read and process sensor signals; (g) setup of part of the assembly of a hybrid 2D pixel detector [246, 257]: each p–i–n-diode pixel, which is soldered to a separate cell of the processing circuit matrix using a microsphere of fusible indium solder, operates as a separate full-fledged point p–i–n diode detector.

Technologies have been developed based on the principle of p–i–n diodes shown in Fig. 28a, which are designed to manufacture [247, 248] silicon sensors for linear microstrip [28, 29, 237, 239] and 2D pixel detectors [30, 237, 246, 254–256] (Figs 28b, d).

The standard single silicon p–i–n diode (Fig. 28a) is a semiconductor device manufactured using planar technology [28, 247, 248, 253] on a thin (a few hundred micrometers thick) single-crystal high-resistance silicon wafer (resistivity up to 4 kΩ cm). The opposite sides of the wafer are heavily doped: one to high n-type conductivity, the other to p-type conductivity, and between these regions there remains a very depleted layer whose conductivity is close to the intrinsic (i) conductivity of pure silicon.

Modern methods of doping silicon allow obtaining planar p–i–n diodes with an i-layer whose thickness is up to several hundred micrometers (usually ~ 300 – 500 μm), a value sufficient for efficient absorption and detection of X-ray photons [246] in the energy range 4–40 keV. Absorbed X-ray photons generate pairs of electron–hole charge carriers in the depleted layer (Fig. 28a), which, under the effect of the electric field of the p–n junction when a circuit is closed without a power source, can create a photovoltaic electron current proportional to the flux of absorbed X-ray photons (detection in photocurrent mode) [251–253]. Such p–i–n diodes have long been widely used as point semiconductor detectors to measure extremely intense fluxes of X-ray photons [34–36, 253], including even those emerging from undulators and wigglers in SR sources, and they are currently being commercially manufactured. Point X-ray p–i–n diodes with an area of several dozen mm^2 operating in the photocurrent mode are used, for example, to monitor the position of beams in SR sources and in adjusting laboratory X-ray diffractometers [253]. In contrast to gas-filled ionization chambers used for the same purpose, detectors on p–i–n diodes are much smaller and do not require electric power [253].

If a reverse bias voltage of about 100 V is applied to the diode (as shown in Fig. 28a), then the p–i–n-diode detector operates in the photoconductivity mode as a discrete photon counter with an energy resolution [258]. An external electric field separates electron–hole pairs, completely removing charge carriers from the high-resistance layer, to make the depleted working volume very sensitive to ionizing radiation. X-ray photons entering the working volume of the diode are absorbed and form electron–hole pairs in the Si crystal, as shown schematically in Fig. 28. Under the effect of a reverse bias field, the charges move to opposite surfaces of the diode, the holes being recorded as current pulses with the amplitude proportional to the energy of the absorbed photon.

Position-sensitive linear (Fig. 28b) and 2D pixel (Fig. 28d) sensors are produced by forming a ruler or matrix of regularly spaced identical p–i–n diodes located on one single-crystal wafer whose conductivity is close to the intrinsic conductivity of a pure defect-free semiconductor. The first commercially produced and most widespread detectors of this type today are silicon 1D strip and 2D pixel detectors, although attempts have recently been made to develop similar detectors based on other semiconductors [246] in order to expand the spectral range sensitivity to hard X-rays and enhance energy resolution and operation speed. The advantage of silicon in this competition lies in the high level of development of silicon semiconductor technology and the availability of single-crystal Si wafers of high perfection and large area.

Depending on the research task, both 2D and 1D detectors are used in X-ray diffraction experiments. To record an X-ray picture with axial symmetry, for example, powder diffraction patterns, there is often no need to obtain a 2D or spatial image, and it suffices to produce only one cross section of this image. It is more convenient in this case to use a linear position-sensitive detector, whose design is simpler, size significantly smaller, and cost much lower compared with similar 2D detectors. Therefore, in parallel with 2D pixel semiconductor detectors, the production of 1D detectors for X-ray powder diffractometry is developing [239, 259–261]. The technology to manufacture these two types of position-sensitive detectors varies significantly, but the principle of operation is similar, as are their main technological characteristics, including speed, radiation resistance, and spatial and energy resolution.

One-dimensional position-sensitive X-ray detectors were actively developed and applied in powder X-ray diffractometry in the last three decades of the 20th century. Gas-discharge proportional counters of various designs were primarily used as these detectors [34–36, 49]; They were bulky and easily damaged by radiation. Microstrip or strip detectors developed for elementary particle physics [28, 29] turned out to be more attractive for X-ray diffractometry than a number of other types of linear coordinate-sensitive X-ray detectors [34–36, 49, 218, 239, 259] due to the high accuracy of determining the coordinates of the photon, the rather high energy resolution inherent in semiconductor detectors, the wide dynamic range, the almost complete absence of intrinsic noise, and high resistance to the effects of a direct X-ray beam that is characteristic of silicon $p-i-n$ diodes.

The microstrip detector [28, 237] is a series of narrow $p-i-n$ diodes placed on a single semiconductor single-crystal wafer (Fig. 28b). The basis of the detector is a thin (~ 300–500 μm) wafer of single-crystal high-resistance silicon with n-type conductivity, which is the working medium of the detector. Thin strips of metal electrodes (strips) are arranged on one of the wafer's planes to collect signal current (holes), spaced apart by a distance of ≈ 20 μm, while the opposite plane is covered with a continuous micrometer-thick metal layer, for example, of aluminum, which collects the flux of electrons. To prevent spontaneous injection of electrons from the metal into the working volume of the detector, layers with an increased hole concentration (p^+) are implanted under metal collector electrodes, as shown in Fig. 28b. A layer of heavily doped n-type silicon is formed on the opposite plane of the detector plate (n^+ layer).

Each strip of a collector electrode with an implanted p-type region, plus a depleted Si layer, plus an implanted n-type region with a metal electrode is actually a semiconductor $p-i-n$ diode, and all strips form a 1D array of such semiconductor diodes located with constant pitch along the length of the Si crystal. The width of the electrode strips and the distance between the strips primarily determine the spatial resolution of the detector.

For the detector to operate in the discrete quantum counter mode, the complete depletion voltage is applied between the n^+ and p^+ layers, which is a reverse electrical bias (usually $V \geqslant 100$ V) whose magnitude is sufficient to ensure complete displacement of all charge carriers from the detector working volume and extend the region of depletion in the main carriers to the entire thickness of high-resistance Si, i.e., to make it an i-type semiconductor [28, 29]. Similarly to the considered case of a single $p-i-n$ diode, the X-ray photons entering the detector working volume are absorbed and produce electron–hole pairs in the depleted Si crystal (Fig. 28b). Charges from electron–hole pairs generated by an absorbed X-ray photon are separated by an electric field applied to the detector and move to opposite surfaces: holes go to the nearest collector read electrodes, where pulses of their current and spatial coordinates of the recording strips are recorded, while the electrons are collected on the common electrode on the opposite side of the single-crystal plate.

The spatial resolution of microstrip detectors is as high as 10 μm, and the time resolution is 10^{-8} s, a value that is several orders of magnitude higher than that of scintillation counters that are still used in X-ray diffractometry. Silicon microstrip detectors and $p-i-n$ diodes have a very low intrinsic noise at room temperature and are extremely resistant to radiation [28, 29, 34–36, 237, 239], unlike most X-ray detectors.

Short linear strip solid-state detectors have recently become widely used also in powder diffractometers with a focusing geometry, such as Bragg–Brentano devices [239, 259], to speed up the collection of XRD data. The first detectors of this type appeared and were tested on powder diffractometers at the beginning of the 21st century. Tests in [239] showed their very high efficiency. The X'Celerator microstrip detector developed by PANalytical for the X'Pert PRO diffractometer series [239] (Fig. 28c) provides a 100-fold increase in the measurement speed. This implies that the acquisition of diffraction data, which previously required three hours of scanning, can now be completed in less than two minutes without degrading the angular resolution. Almost all laboratory X-ray powder diffractometers supplied by leading manufacturers have recently been equipped with similar detectors.

The main and most impressive result of switching to semiconductor detector technologies based on the principle of $p-i-n$ diodes in X-ray experiments was obtained from the creation of 2D silicon detectors that are widely used not only in X-ray diffractometry [219] but also in modern medical and engineering radiography, something that can hardly be imagined now without them. Owing to the advantages of $p-i-n$ diode silicon detectors noted above, semiconductor pixel detectors have recently superseded and replaced 2D CCD detectors with a fluorescent sensor both in SR sources and in laboratory X-ray diffractometers with XRTs.

Two technologies for the production of semiconductor 2D ionization matrix pixel detectors are being developed in parallel [247, 248, 257]: hybrid detectors and monolithic detectors. These two competing technologies are based on the same principle, but are structurally different. Detectors of the first type — hybrid detectors — consist of two different parts connected together in a contact way (an X-ray sensor and a chip for reading electric signals), while monolithic detectors are made as an assembly with a signal processing chip (usually a dedicated custom-made CCD integrated circuit) on one Si crystal, which at the same time operates as a sensor of X-ray photons. The performance of monolithic detectors is much higher by design than that of hybrid ones. However, a difficult problem arises in their production that is related to the choice of semiconductor material and the efficiency of the sensor, the latter often being sacrificed for the sake of optimizing the processing chip. In hybrid detectors, both the sensor and the processing chip can be selected in an optimal way, although the signal transfer rate, i.e., performance, degrades due to the pairing of several different materials. Therefore, hybrid technology is leading the way in the manufacture of 2D semiconductor detectors, based on which hybrid pixel array detectors (HPADs) are manufactured [244]. A revolutionary moment in the entrenchment of this technology was the development of a method (Fig. 28c) for the element-wise soldered connection of silicon microsensors with micropixels of a reading and processing integrated matrix chip [249, 254].

The first HPADs to appear in X-ray diffractometry were the PILATUS [3] semiconductor pixel hybrid X-ray photon counters created at the Paul Scherrer Institute (PSI, Switzerland) [237, 238] to be operated on SLS, a Swiss SR source. The first version of this type of detector, which consists of an array of X-ray semiconductor p–i–n diode microsensors each of which is rigidly connected to a separate cell of a dedicated processing chip, was created at PSI in 2001. Currently, DECTRIS, a company affiliated with the PSI Institute, produces a number of models of PILATUS 100K/200K/300K/6M detectors and more recent models [250] that differ in the receiving window size, pixel sizes, overall dimensions, and weight. The most suitable in size and weight (~ 4 kg) for laboratory X-ray installations are the PILATUS 100K (Fig. 28e) and 200K detectors [30].

PILATUS semiconductor hybrid pixel detectors [30, 237, 238, 256] (Figs 28d–e) consist of a 2D array of microscopic semiconductor p–i–n diodes (X-ray sensors) made using planar technology from high resistivity silicon soldered to the pixels of a readout dedicated integrated circuit (ASIC). A 2D pixel semiconductor Si detector operates in the same way as the strip detector considered above, the only difference being that the position of the recording implanted p^+ regions in it is characterized by not one but two coordinates. Each hybrid element of the resulting matrix is a full-fledged semiconductor counter of photons that converts their energy immediately into an electrical signal. The detector has the energy resolution $\Delta\varepsilon \approx 500$ eV, which is sufficient, for example, to distinguish the K_α line in the characteristic radiation spectrum of an XRT and exclude the K_β line from recording without using a metal filter. The quantum efficiency of the PILATUS 100K detector is close to 100% for photons with an energy of 8 keV and $\sim 50\%$ for 17.5 keV. The pixel size of the p–i–n diode sensor array, which is the same as the cell size of the processing integrated chip, is 172×172 μm. The area of the detector receiving window is 83.8×33.5 mm. The signal transmission factor is close to 100%, and the maximum counting rate is 2×10^6 photon s^{-1} pixel^{-1}, which, per unit area of the receiving window, is thousands of times higher than the maximum count rate of 'point' scintillation detectors, which had previously been the most popular devices used in X-ray single-crystal diffractometry. This detector has no pixel spreading, there is virtually no intrinsic background (noise), and p–i–n diode sensors feature very high radiation resistance and can withstand long (hundreds of hours) exposure to direct radiation beams from XRTs and even SR beams without damage. Radiation resistance this high is a huge benefit and advantage of the new hybrid silicon detectors compared to most counters of quanta of previous generations.

In performing XRD analysis of single crystals with a PILATUS detector, the crystal can be rotated continuously without opening and closing the beam shutter; in the process of data transmission, the detector simply disables recording. Data are collected at a rate of 3 s per frame, and processing and reading data only take 3 ms! The readout time of 3 ms is very short compared with the exposure time, and the information gaps associated with it do not impair data quality [255]. Most important, unlike CCD detectors, the PILATUS detector does not add its intrinsic noise to the data.

Owing to the outstanding technological characteristics, many manufacturers of diffractometers, and not only single-crystal ones (for example, Bruker AXS, PANalytical, Rigaku Oxford Diffraction, and Stoe (Germany)), have recently [31] been equipping their devices [262] with hybrid pixel silicon detectors similar to PILATUS detectors.

Two-dimensional detectors proved to be very useful in powder diffractometry in measuring diffraction profiles of total scattering and in diffraction experiments for structural analysis of conditionally crystalline materials in accordance with the Debye formula [3,18, 226–228]. For example, collecting data using the pair distribution method (PDF) by means of a point detector on a synchrotron may require scanning diffraction angles for up to 24 hours, while a 2D detector can do this job in a fraction of a second [226]. Another advantage of 2D detectors is that the texture can be studied, and its distorting effects can be corrected when measuring the intensity of the Bragg lines from the Debye rings, because the 2D detector records the intensity depending on both the angle 2θ and the azimuthal angle. Integration of 2D detector data as a function of both the azimuthal angle and 2θ is now a common practice in X-ray powder diffractometry [220].

The use of 2D hybrid pixel detectors in various methods of diffraction measurements of single crystals, powders, and thin films [224, 263] is actively promoted by the Rigaku Oxford Diffraction Corporation, which has been equipping its single-crystal X-ray diffractometers [262] for more than 5 years with the PILATUS3 R 200K detectors [https://www.rigaku.com/en/products/protein/pilatus200k]. In 2013, Rigaku launched production of its own HyPix-3000 semiconductor hybrid pixel detector [264]. According to the technological characteristics [264], the HyPix-3000 detector is very similar to the PILATUS 100K: it has a window with an active area of about 3000 mm^2 (77.5×38.5 mm compared with 83.8×33.5 mm for PILATUS); however, its pixel sizes are almost half the size (100 μm), i.e., the spatial resolution is two times higher, and the maximum count rate per pixel is about 10^6 photon s^{-1}. An attractive feature of the HyPix-3000 detector is that it not only can be used as a 2D detector

---

[3] PILATUS, the name of a series of detectors, which sounds similar to the name of the prefect of ancient Rome's Judea at the beginning of the first millennium A.D. has actually no relation to it whatsoever and is a kind of abbreviation of the full name of the series: PIxeL ApparaTUs for the SLS, where SLS (Swiss Light Source) is the name of the Switzerland-based SR source.

with high spatial resolution, no intrinsic noise, and high counting speed, but also operates in the modes of a 1D linear detector and zero-dimensional point detector.

7. Conclusion

At the end of the 20th and beginning of the 21st centuries, we witnessed rapid improvement of tools intended for X-ray diffractometry, the main method of structural analysis of matter in condensed state. This progress affected all the main components of X-ray diffractometers: radiation sources, X-ray optical elements, and X-ray detectors.

The central point of this development is undoubtedly associated with achievements in creating ultra-bright sources of X-ray radiation. Improvement of SR sources, which appeared at the end of the 20th century and for over two and a half decades have evolved from first-generation sources to dedicated third-generation storage rings, and advances in technology of free-electron X-ray lasers based on linear accelerators have demonstrated the possibility of a tremendous increase in the brightness of X-ray sources. Over the 100 years since the emergence of the first X-ray tube, the brightness of X-ray sources has increased by only 10^6 times, while over the past 20 years, owing to third-generation SR sources and XFELs, the brightness of X-ray sources has increased by 10^{20} times! However, the high cost of SR sources makes them accessible to only a small part of the community of specialists working with X-ray radiation. These devices are used primarily in basic science and are inaccessible for solving analytical problems. The desire to make such X-ray sources more accessible for specialists stimulated the development of less expensive and less bulky radiation sources with similar characteristics.

Fundamentally new sources of X-rays with unprecedented high brightness were created at the end of the 20th and beginning of the 21st centuries [68, 71, 74, 96, 98, 106]. High-transmission reflective X-ray optical devices [22–24, 265] for cleaning, monochromatizing, focusing, and collimating X-ray beams emerged that can be used not only for SR but also in laboratory diffractometers with XRTs. Owing to these X-ray optical devices combined with the latest microfocusing XRTs [214, 215, 266], commercial production of inexpensive and highly efficient ultra-bright X-ray sources [177, 193, 204, 266] and their wide use for laboratory X-ray diffractometers commenced. Finally, the technology was implemented to manufacture solid-state semiconductor coordinate-sensitive linear and 2D X-ray detectors [250, 254–257, 259]. They feature high sensitivity and quantum efficiency, high speed and amplitude energy resolution, a nearly zero level of intrinsic noise, and resistance to radiation to the extent that they are not damaged even if exposed for a long time to a direct beam from an XRT. The use of such detectors fundamentally changed the approach to experiments on diffraction studies of single crystals, powders, and noncrystalline materials and increased the speed of data collection for X-ray structural analysis by several times.

The new analytical equipment for XRD studies that has appeared in the last decade has enabled routinely using the methods of analysis of materials that had previously been of primarily academic interest but could not be widely used due to lack of technological capabilities; measurements of diffraction patterns of total scattering and studies of the structure of thin films by a sliding beam of X-ray radiation are the examples. The time needed for data collection for single-crystal XRD analysis has been significantly reduced, and, most importantly, the accuracy and reliability of structural analysis have been boosted.

The increased brightness of radiation sources is undoubtedly a very important consequence of the development of X-ray research methods; however, in the process of this development, sources with a unique time structure have emerged, such as synchrotron storage rings, XFELs [71, 77, 85, 87–91], Compton backscattering sources [113–115], and LP X-ray sources [116, 117, 135, 149, 162]. The emergence of pulsed radiation sources with a pronounced time structure has expanded the field of XRD applications to studying the structure in dynamics, with a time resolution up to femtoseconds. Technological advances of the last two decades in the field of X-ray sources have made such studies possible not only in resource-sharing centers in SR or XFEL sources but also in university and academic laboratories and in medical institutions.

While we can confidently assert today that modern X-ray diffractometry for structural analysis and diffraction methods for measuring the structure of materials have greatly surpassed the capacities of the instruments that were available in the mid-1980s, the information presented in this review suggests that over the next decade achievements in the study of the structural dynamics of matter by ultrafast XRD both in the gas phase and in condensed form will be no less impressive.

We note that the improvement in X-ray methods continues, especially in the field of radiation sources. As was stressed in this review, it has been possible over the past 20 years to increase the brightness of X-ray sources by 10^{20} times owing to gigantic modern XFELs. Such significant progress may presumably be achieved in the foreseeable future also in the field of relatively compact radiation sources suitable for laboratory use. Trends of this development are already visible. For example, competitors of modern XFELs, which are currently the brightest sources of X-rays, are starting to appear. The giant machines based on multi-gigawatt electron accelerators and the longest magnetic plug-in devices such as undulators are very likely to be challenged by the LP electron accelerators discussed in Sections 3.6 and 3.7.

The use of ultrashort laser-radiation sources made it possible to radically change the standard approaches to the study of matter by means of synchronized pulses of ultra-bright X-ray radiation and thus achieve high space-time resolution. The concept of using ultrashort laser pulses in combination with electronic optical devices, supported by the development of pulsed laser technology and the advent of commercially available and sufficiently reliable femtosecond lasers, has created important preconditions for achieving resolutions of several dozen femtoseconds, a value that is comparable to a characteristic period of oscillations of atoms in molecules. Once this frontier is crossed, the creation of a 'molecular cinema' will become a reality: it will be possible to observe the dynamics of atoms in the space–time continuum, which, apart from purely academic interest, is of great practical importance.

Acknowledgments

The author is grateful to L A Aslanov (Faculty of Chemistry, Lomonosov Moscow State University) and A A Ischenko (MIREA — Russian Technological University) for the valuable discussions, advice, and ongoing support in writing the review.

References

1. Chung F H, Smith D K (Eds) *Industrial Application of X-Ray Diffraction* (New York: Marcel Dekker, 2000)
2. Mittemeijer E J, Scardi P (Eds) *Diffraction Analysis of the Microstructure of Materials* (Berlin: Springer, 2004)
3. Dinnebier R E, Billinge S J L (Eds) *Powder Diffraction*: *Theory and Practice* (Cambridge: Royal Society of Chemistry, 2008)
4. Mittemeijer E J, Welzel U (Eds) *Modern Diffraction Methods* (New York: Wiley-VCH Verlag, 2013) https://doi.org/10.1002/9783527649884
5. Kumar C S S R (Eds) *X-Ray and Neutron Techniques for Nanomaterials Characterization* (New York: Springer, 2016)
6. Friedrich W, Knipping P, von Laue M *Sitzungsberichte Kgl. Bayer. Akad. Wiss.* 303 (1912); reprinted: *Naturawissenschaften* **39** 361 (1952)
7. von Laue M *Sitzungsberichte Kgl. Bayer. Akad. Wiss.* 363 (1912)
8. Bragg W H, Bragg W L *Proc. R. Soc. London A* **88** 428 (1913)
9. Bragg W H *Phil. Trans. R. Soc.* **215** 253 (1915)
10. Wulf G *Phys. Z.* **14** 217 (2013); Translated into Russian: *Izbrannye Trudy po Kristallofizike i Kristallografii* (Moscow–Leningrad: GITTL, 1952) p. 326
11. Guinier A *Theorie et Technique de la Radiocristallographie* 2nd ed. (Paris: Dunod, 1956); Translated into Russian: *Rengtgenografiya Kristallov. Teoriya i Praktika* (Moscow: GIFML, 1961)
12. Warren B E *X-Ray Diffraction* (Reading, Mass.: Addison-Wesley Publ. Co., 1969)
13. Klug H P, Alexander L E *X-Ray Diffraction Procedures for Polycrystalline and Amorphous Materials* 2nd ed. (New York: John Wiley, 1974)
14. Arndt U W, Wonacott A J *The Rotation Method in Crystallography* (Amsterdam: North-Holland Publ. Co., 1977)
15. Porai-Koshits M A *Osnovy Strukturnogo Analiza Khimicheskikh Soedinenii* (Basics of the Structural Analysis of Chemical Compounds) (Moscow: Vysshaya Shkola, 1989)
16. Blake A J et al. *Crystal Structure Analysis*: *Principles and Practice* (Ed. W Clegg) 2nd ed. (New York: Oxford Univ. Press, 2009)
17. Pecharsky V K, Zavalij P Y *Fundamental of Powder Diffraction and Structural Characterization of Materials* 2nd ed. (Berlin: Springer, 2009)
18. Egami T, Billinge S J L *Underneath the Bragg Peaks*: *Structural Analysis of Complex Materials* 2nd ed. (Amsterdam: Elsevier, 2012)
19. Sattler K D (Ed.) *Handbook of Nanophysics*: *Principles and Methods* (Boca Raton, Fl.: Taylor and Francis Group, CRC Press, 2011)
20. Ischenko A A, Fetisov G V, Aslanov L A *Nanosilicon*: *Properties, Synthesis, Applications, Methods of Analysis and Control* (Boca Raton, Fl.: CRC Press, 2015)
21. Michaelsen C et al. *Adv. X-Ray Anal.* **42** 308 (2000)
22. Kumakhov M A *Proc. SPIE* **4155** 2 (2000)
23. Bilderback D H *X-Ray Spectrom.* **32** 195 (2003)
24. Hertlein F et al. *Part. Part. Syst. Charact.* **22** 378 (2006)
25. Shimizu K, Omote K *Rigaku J.* **24** 1 (2008)
26. Wohlschlögel M et al. *J. Appl. Cryst.* **41** 124 (2008)
27. Mundboth K et al. *J. Synchrotron Rad.* **21** 16 (2014)
28. Sandukovskii V G, Savel'ev V I *Fiz. Elem. Chast. At. Yad.* **22** 1347 (1991)
29. Chilingarov A G *Fiz. Elem. Chast. At. Yad.* **23** 785 (1992)
30. User Manual PILATUS Detector Systems. Version 1.2, Dectris Ltd. 06.02.2009
31. Skarzynski T *Acta Cryst. D* **69** 1283 (2013)
32. Dauter Z, Jaskolski M, Wlodawer A *J. Synchrotron Rad.* **17** 433 (2010)
33. Duke E M H, Johnson L N *Proc. R. Soc. Lond. A* **466** 3421 (2010)
34. Fetisov G V *Sinkhrotronnoe Izluchenie. Metody Issledovaniya Struktury Veshchestv* (Synchrotron Radiation. Methods for Studying Structure of Substances) (Moscow: Fizmatlit, 2007)
35. Zakharova E V *Phys. Usp.* **50** 767 (2007); *Usp. Fiz. Nauk* **177** 803 (2007) see information about the book [34]
36. Bolotina N B *Crystallogr. Rev.* **15** 143 (2009)
37. Clarck S M *Crystallogr. Rev.* **8** 57 (2002)
38. Dong Y-H et al. *J. Appl. Cryst.* **36** 1123 (2003)
39. Buras B et al., in *International Tables for Crystallography* (Ed. E Prince) 3rd ed. (Dordrecht: D. Reidel Publ. Co., 2004) p. 84
40. Kämpfe B, Luczak F, Michel B *Part. Part. Syst. Charact.* **22** 391 (2005)
41. Leng Y *Materials Characterization*: *Introduction to Microscopic and Spectroscopic Methods* (Singapore: John Wiley and Sons, 2008)
42. Porai-Koshits M A *Prakticheskii Kurs Rentgenostrukturnoga Analiza* (Practical Course of X-ray Structural Analysis) Vol. 2 (Moscow: Izd. MGU, 1960)
43. Glatter O, Kratky O (Eds) *Small Angle X-Ray Scattering* (New York: Academic Press, 1982)
44. Feigin L A, Svergun D I *Structure Analysis by Small-Angle X-Ray and Neutron Scattering* (New York: Plenum Press, 1987); Translated from Russian: Svergun D I, Feigin L A *Rentgenovskoe i Neitronnye Malouglovoe Rasseyanie* (Moscow: Nauka, 1986)
45. Helliwell J R *Macromolecular Crystallography with Synchrotron Radiation* (Cambridge: Cambridge Univ. Press, 1992)
46. Young R A (Ed.) *The Rietveld Method* (Oxford: Oxford Univ. Press, 1995)
47. Ren Z et al. *J. Synchrotron Rad.* **6** 891 (1999)
48. Will G *Powder Diffraction*: *The Rietveld Method and the Two Stage Method to Determine and Refine Crystal Structures from Powder Diffraction Data* (Berlin: Springer, 2006)
49. Aslanov L A, Fetisov G V, Howard J A K *Crystallographic Instrumentation* (Oxford: Oxford Univ. Press, 1998)
50. Chernyshev V V *Russ. Chem. Bull.* **50** 2273 (2001); *Izv. Ross. Akad. Nauk. Ser. Khim.* (12) 2174 (2001)
51. Ladd M, Palmer R *Structure Determination by X-Ray Crystallography. Analysis by X-Rays and Neutrons* 5th ed. (New York: Springer, 2013)
52. Fawcett T et al. *Powder Diffr.* **32** 63 (2017)
53. Billinge S J L, Thorpe M F (Eds) *Local Structure from Diffraction* (New York: Kluwer Acad. Publ., 2002)
54. Pyt'ev Yu P, Shishmarev I A *Kurs Teorii Veroyatnostei i Matematicheskoi Statistiki dlya Fizikov* (Course of Probability Theory and Mathematical Statistics for Physicists) (Moscow: Izd. MGU, 1983)
55. Borek D, Minor W, Otwinowski Z *Acta Cryst. D* **59** 2031 (2003)
56. Wilson A J C, in *International Tables for Crystallography* Vol. C, 1st online ed. (Dordrecht: D. Reidel Publ. Co., 2006) p. 666
57. Fetisov G V, in *Analiticheskaya Khimiya i Fiziko-Khimicheskie Metody Analiza* (Analytical Chemistry and Physicochemical Analytical Methods) Vol. 2 (Ed. A A Ischenko) 2nd ed. (Moscow: Academia, 2012) p. 153
58. Coolidge W D *Phys. Rev.* **2** 409 (1913)
59. Coolidge W D, Dempster L E, Tanis H E (Jr.) *Physics* **1** 230 (1931)
60. Als-Nielsen J, McMorrow D *Elements of Modern X-Ray Physics* 2nd ed. (New York: John Wiley and Sons, 2011)
61. Ternov I M *Phys. Usp.* **38** 409 (1995); *Usp. Fiz. Nauk* **165** 429 (1995)
62. Potylitsyn A P, Vnukov I E, in *Electron–Photon Interaction in Dense Media* (Ed. H Wiedemann) (Berlin: Springer, 2002) p. 25
63. Baryshevsky V G, Feranchuk I D, Ulyanenkov A P *Parametric X-Ray Radiation in Crystals*: *Theory, Experiment and Applications* (Berlin: Springer, 2005)
64. Miaja-Avila L et al. *Struct. Dyn.* **2** 024301 (2015)
65. Brenner C M et al. *Plasma Phys. Control. Fusion* **58** 014039 (2016)
66. Mills D M et al. *J. Synchrotron Rad.* **12** 385 (2005)
67. Attwood D, Sakdinawat A *X-Rays and Extreme Ultraviolet Radiation*: *Principles and Applications* (Cambridge: Cambridge Univ. Press, 2017)
68. Mobilio S, Boscherini F, Meneghini C (Eds) *Synchrotron Radiation. Basics, Methods and Applications* (Berlin: Springer, 2015)
69. Guinebretière R *X-Ray Diffraction by Polycrystalline Materials* (New York: Wiley, 2007) https://doi.org/10.1002/9780470612408
70. Wiedemann H *Synchrotron Radiation* (Berlin: Springer, 2003)
71. Jaeschke E et al. (Eds) *Synchrotron Light Sources and Free-Electron Lasers. Accelerator Physics, Instrumentation and Science Applications* (Berlin: Springer, 2016)
72. Thompson A C et al., X-Ray Data Booklet (LBNL/PUB-490 Rev. 3) 3rd ed. (Berkeley, Calif.: Lawrence Berkeley National Laboratory Univ. of California, 2009); http://xdb.lbl.gov/xdb-new.pdf
73. Robinson A, X-Ray Data Booklet (LBNL/PUB-490 Rev. 3) 3rd ed. (Ed. A C Thompson) (Berkeley, Calif.: Lawrence Berkeley National Laboratory Univ. of California, 2009) pp. 2 – 21
74. Lightsources.org Collab. Light sources of the world, https://lightsources.org/lightsources-of-the-world/

75. Siffalovic P et al., in *X-Ray and Neutron Techniques for Nanomaterials Characterization* (Ed. C S S R Kumar) (Berlin: Springer-Verlag, 2016) p. 507
76. Hemberg O, Otendal M, Hertz H M *Appl. Phys. Lett.* **83** 1483 (2003)
77. Geloni G, Huang Z, Pellegrini C, in *X-Ray Free Electron Lasers: Applications in Materials, Chemistry and Biology* (Energy and Environment Series, No. 18, Eds U Bergmann, V K Yachandra, J Yano) (London: The Royal Society of Chemistry, 2017) p. 3
78. Leoni M, Welzel U, Scardi P *J. Res. Natl. Inst. Standards Technol.* **109** 27 (2004)
79. Leoni M, in Ischenko A A, Fetisov G V, Aslanov L A *Nanosilicon. Properties, Synthesis, Applications, Methods of Analysis and Control* (Ischenko A A, Fetisov G V, Aslanov L A) (Boca Raton, FL: CRC Press, 2015) p. 519
80. James R W *The Optical Principles of the Diffraction of X-Rays* (London: G. Bell and Sons, 1948); Translated into Russian: *Opticheskie Printsipy Difraktsii Rentgenovskikh Luchei* (Moscow: IL, 1950)
81. Coppens P et al. *Synchrotron Radiation Crystallography* (London: Academic Press, 1992)
82. Kulipanov G N *Phys. Usp.* **50** 368 (2007); *Usp. Fiz. Nauk* **177** 384 (2007)
83. Margaritondo G, in *Synchrotron Radiation. Basics, Methods and Applications* (Eds S Mobilio, F Boscherini, C Meneghini) (Berlin: Springer, 2015) p. 29
84. Wiedemann H *Particle Accelerator Physics* (Berlin: Springer-Verlag, 2007)
85. Pellegrini C, Stöhr J *Nucl. Instrum. Meth. Phys. Res. A* **500** 33 (2003)
86. Kurilko V I, Tkach Yu V *Phys. Usp.* **38** 231 (1995); *Usp. Fiz. Nauk* **165** 241 (1995)
87. Huang Z, Kim K-J *Phys. Rev. ST Accel. Beams* **10** 034801 (2007)
88. Emma P et al. *Nature Photon.* **4** 641 (2010)
89. Yabashi M, Tanaka H, Ishikawa T *J. Synchrotron Rad.* **22** 477 (2015)
90. Kim K-J et al., in *Proc. of the Intern. Particle Accelerator Conf. IPAC'16, Busan, Korea, May 8–13, 2016*, p. 801, paper MOPOW039
91. Madsen A, Sinn H *CERN Courier* **57** (6) 19 (2017)
92. Kim K-J, Shvyd'ko Yu, Reiche S *Phys. Rev. Lett.* **100** 244802 (2008)
93. Kim K-J, Shvyd'ko Yu V *Phys. Rev. ST Accel. Beams* **12** 030703 (2009)
94. Li K, Deng H *Nucl. Instrum. Meth. Phys. Res. A* **895** 40 (2018)
95. Chergui M, Collet E *Chem. Rev.* **117** 11025 (2017)
96. The European XFEL in International Comparison, https://www.xfel.eu/facility/comparison/index_eng.html
97. Schmüser P et al. *Free-Electron Lasers in the Ultraviolet and X-Ray Regime* (Berlin: Springer, 2014)
98. Huang Z, Ingolf L *Nature Photon.* **6** 505 (2012)
99. Ishikawa T et al. *Nature Photon.* **6** 540 (2012)
100. The European XFEL Overview, https://www.xfel.eu/facility/overview/index_eng.html
101. Von der Linde D et al. *Laser Part. Beams* **19** 15 (2001)
102. Jaroszynski D A et al. *Phil. Trans. R. Soc. Lond. A* **364** 689 (2006)
103. Gauthier J-C, in *Progress in Ultrafast Intense Laser Science* Vol. 1 (Berlin: Springer, 2006) p. 151
104. Tsipenyuk Yu M *Fundamental'nye i Prikladnye Issledovaniya na Mikrotrone* (Basic and Applied Research on Microtron) (Moscow: Fizmatlit, 2009)
105. CORDIS: Final Report — LABSYNC, Laboratory compact light sources. Project ID: 213126. Belgium, 2012, http://cordis.europa.eu/result/rcn/54953_en.html
106. Yamada H et al., in *Comprehensive Biomedical Physics* Vol. 8 (Ed. A Brahme) (Amsterdam: Elsevier, 2014) p. 43
107. Lobko A S *Eksperimental'nye Issledovaniya Parametricheskogo Rentgenovskogo Izlucheniya* (Experimental Studies of Parametric X-ray Radiation) (Minsk: BGU, 2006)
108. Minkov D A, Yamada H *Annu. J. Electron.* 166 (2014)
109. Yamada H et al. *Proc. SPIE* **7078** 70780P (2008)
110. Yamada H *J. Synchrotron Rad.* **5** 1326 (1998)
111. Yamada H *AIP Conf. Proc.* **716** 12 (2004)
112. Polyakov S N et al. *Proc. SPIE* **10243** 102430Y (2017)
113. Eggl E et al. *J. Synchrotron Rad.* **23** 1137 (2016)
114. Artyukov I A et al. *Laser Part. Beams* **34** 637 (2016)
115. Artyukov I A et al. *J. Phys. Conf. Ser.* **784** 012002 (2017)
116. Pfeifer T, Spielmann C, Gerber G *Rep. Prog. Phys.* **69** 443 (2006)
117. Macchi A *A Superintense Laser-Plasma Interaction Theory Primer* (Berlin: Springer, 2013)
118. Walker P A et al. *J. Phys. Conf. Ser.* **874** 012029 (2017)
119. Jaroszynski D A, Vieux G *AIP Conf. Proc.* **647** 902 (2002)
120. Leemans W P et al. *Nature Phys.* **2** 696 (2006)
121. Leemans W, Esarey E *Phys. Today* **62** (3) 44 (2009)
122. Leemans W P et al., in *Particle Accelerator Conf., PAC'11*, p. 1416, paper WEOBS1
123. Leemans W P et al. *Phys. Rev. Lett.* **113** 245002 (2014)
124. Esarey E, Schroeder C B, Leemans W P *Rev. Mod. Phys.* **81** 1229 (2009)
125. Corde S et al. *Rev. Mod. Phys.* **85** 1 (2013)
126. Malka V, in *Laser-Plasma Interactions and Applications* (Eds P McKenna et al.) (Berlin: Springer, 2013) p. 281
127. Wang X et al. *Nature Commun.* **4** 1988 (2013)
128. Rini M *Physics* **7** 126 (2014)
129. Kostyukov I Yu, Pukhov A M *Phys. Usp.* **58** 81 (2015); *Usp. Fiz. Nauk* **185** 89 (2015)
130. Maier A R, Kirchen M, Grüner F, in *Synchrotron Light Sources and Free-Electron Lasers* (Eds E Jaeschke et al.) (Cham: Springer, 2016) p. 225
131. Giulietti D, Gizzi L A *Riv. Nuovo Cimento* **21** 1 (1998)
132. Artsimovich L A, Sagdeev R Z *Fizika Plazmy dlya Fizikov* (Plasma Physics for Physicists) (Moscow: Atomizdat, 1979)
133. Rousse A et al. *Phys. Rev. E* **50** 2200 (1994)
134. Jiang Z et al. *Phys. Plasmas* **2** 1702 (1995)
135. Schwoerer H, in *Femtosecond Technology for Technical and Medical Applications* (Eds F Dausinger, F Lichtner, H Lubatschowski) (Berlin: Springer-Verlag, 2004) p. 235
136. Gibbon P *Short Pulse Laser Interactions with Matter: An Introduction* (London: Imperial College Press, 2005)
137. Tsukerman V A, Tarasova L V, Lobov S I *Sov. Phys. Usp.* **14** 61 (1971); *Usp. Fiz. Nauk* **103** 319 (1971)
138. Mead S W et al. *Appl. Opt.* **11** 345 (1972)
139. Mallozzi P J et al. *J. Appl. Phys.* **45** 1891 (1974)
140. Rumsby P T *J. Microsc.* **138** 245 (1985)
141. Vinogradov A V, Shlyaptsev V N *Sov. J. Quantum Electron.* **17** 1 (1987); *Kvantovaya Elektron.* **14** 5 (1987)
142. Gamalii E G, Rozanov V B, in *Fizicheskaya Entsiklopediya* (Encyclopedia of Physics) (Ed.-in-Chief A M Prokhorov) Vol. 2 (Moscow: Sovetskaya Entsiklopediya, 1990) p. 552
143. Andreev A A, Yashin V E, Charukhchev A V *Phys. Usp.* **42** 66 (1999); *Usp. Fiz. Nauk* **169** 72 (1999)
144. Wharton K B et al. *Phys. Rev. E* **6402** 025401(R) (2001)
145. Ishchenko A A et al. *Phys. Usp.* **57** 633 (2014); *Usp. Fiz. Nauk* **184** 681 (2014)
146. Ischenko A A, Weber P M, Miller R J D *Russ. Chem. Rev.* **86** 1173 (2017); *Usp. Khim.* **86** 1173 (2017)
147. Ischenko A A *Struktura i Dinamika Svobodnykh Molekul i Kondensirovannogo Veshchestva* (Structure and Dynamics of Free Molecules and Condensed Matter) (Moscow: Fizmatlit, 2018)
148. Ditmire T et al. *Radiat. Phys. Chem.* **70** 535 (2004)
149. Compant La Fontaine A, Courtois C, Lefebvre E *Phys. Plasmas* **19** 023104 (2012)
150. Mulser P, Sigel R, Witkowski S *Phys. Rep.* **6** 187 (1973)
151. Gordienko V M, Savel'ev A B *Phys. Usp.* **42** 72 (1999); *Usp. Fiz. Nauk* **169** 78 (1999)
152. Jiang Y, Lee T, Rose-Petruck C G *J. Opt. Soc. Am. B* **20** 229 (2003)
153. Ledingham K W D et al., arXiv:1106.4152
154. Mourou G A, Tajima T, Bulanov S V *Rev. Mod. Phys.* **78** 309 (2006)
155. Perry M D, Mourou G *Science* **264** 917 (1994)
156. Umstadter D *J. Phys. D* **36** R151 (2003)
157. Joshi C J, Corkum P B *Phys. Today* **48** (1) 36 (1995)
158. Popmintchev T et al. *Science* **336** 1287 (2012)
159. Gibbon P, CERN Yellow Report CERN-2016-001 (Geneva: CERN, 2016); arXiv:1705.10529
160. Elsaesser T, Woerner M *Acta Cryst. A* **66** 168 (2010)
161. Zamponi F et al. *Appl. Phys. A* **96** 51 (2009)
162. Fullagar W et al. *Rev. Sci. Instrum.* **78** 115105 (2007)
163. Bargheer M et al. *Appl. Phys. B* **80** 715 (2005)
164. Edwards R D et al. *Appl. Phys. Lett.* **80** 2129 (2002)
165. Andreev A A et al. *Phys. Rev. E* **65** 026403 (2002)

166. Salzmann D et al. *Phys. Rev. E* **65** 036402 (2002)
167. Andreev A A, Platonov K Yu *Quantum Electron.* **41** 515 (2011); *Kvantovaya Elektron.* **41** 515 (2011)
168. Tajima T, Dawson J M *Phys. Rev. Lett.* **43** 267 (1979)
169. Esarey E et al. *IEEE Trans. Plasma Sci.* **24** 252 (1996)
170. Hooker S M *Nature Photon.* **7** 775 (2013)
171. Stephan F, Krasilnikov M, in *Synchrotron Light Sources and Free-Electron Lasers: Accelerator Physics, Instrumentation and Science Applications* (Eds E J Jaeschke, S Khan, J R Schneider) (New York: Springer, 2016) p. 561
172. Fuchs M et al. *Nature Phys.* **5** 826 (2009)
173. Korn G *Physics* **7** 125 (2014)
174. Loulergue A et al. *New J. Phys.* **17** 023028 (2015)
175. Jenkins R, Snyder R L *Introduction to X-Ray Powder Diffractometry* (New York: Wiley, 1996)
176. Mathieu M, Steier V *Xenocs News Lett.* **8** 1 (2008)
177. Schulz T et al. *J. Appl. Cryst.* **42** 885 (2009)
178. MacDonald C A *X-Ray Opt. Instrum.* **2010** 867049 (2010)
179. MacDonald C A, Owens S M, Gibson W M *J. Appl. Cryst.* **32** 160 (1999)
180. Kumakhov M A *Proc. SPIE* **5943** 59430B (2006)
181. Kumakhov M A *Proc. SPIE* **4765** 20 (2002)
182. Gibson D, Gibson W *Adv. X-Ray Anal.* **45** 286 (2002)
183. Cornaby S et al. *Adv. X-Ray Anal.* **50** 194 (2006)
184. Bjeoumikhov A, Bjeoumikhova S, Wedell R *Part. Part. Syst. Charact.* **22** 384 (2005)
185. Bolotokov A et al. *Analitika* (4) 14 (2012)
186. Arndt U W *J. Appl. Cryst.* **23** 161 (1990)
187. Bjeoumikhov A et al. *X-Ray Spectrom.* **34** 493 (2005)
188. Schields P J et al. *Powder Diffraction* **17** (2) 70 (2002)
189. Hart M, Berman L *Acta Cryst. A* **54** 850 (1998)
190. Schuster M et al. *Proc. SPIE* **3767** 183 (1999)
191. Schuster S M, Göbel H *Adv. X-Ray Anal.* **39** 57 (1997)
192. Yang C, Courville A, Ferrara J D *Acta Cryst. D* **55** 1681 (1999)
193. Wiesmann J et al. *Acta Cryst. A* **66** s291 (2010)
194. Omote K, Harada J *Adv. X-Ray Anal.* **43** 192 (2000)
195. Bergmann A et al. *J. Appl. Cryst.* **33** 869 (2000)
196. Vetterling W T, Pound R V *J. Opt. Soc. Am.* **66** 1048 (1976)
197. Kumakhov M A *Nucl. Instrum. Meth. Phys. Res. B* **48** 283 (1990)
198. Gubarev M et al. *J. Appl. Cryst.* **33** 882 (2000)
199. Engström P et al. *Nucl. Instrum. Meth. Phys. Res. B* **36** 222 (1989)
200. Huang R, Bilderback D H *J. Synchrotron Rad.* **13** 74 (2006)
201. Gillilan R E et al. *J. Synchrotron Rad.* **17** 227 (2010)
202. Arkad'ev V A, Kumakhov M A, Fayazov R F *Sov. Tech. Phys. Lett.* **14** 101 (1988); *Pis'ma Zh. Tekh. Fiz.* **14** 226 (1988)
203. Bushuev V A, Orudzhaliev M N, Kuz'min R N *Vestn. MGU. Ser. 3, Fiz., Astron.* **31** (1) 76 (1990)
204. Bjeoumikhov A et al. *X-Ray Spectrom.* **33** 312 (2004)
205. Engström P et al. *Nucl. Instrum. Meth. Phys. Res. A* **302** 547 (1991)
206. Riekel C et al. *Macromolecules* **30** 1033 (1997)
207. Oosterkamp W J, Philips L *Res. Rep.* **3** 303 (1948)
208. Pankratov E L, Chkhalo N I *High Temp.* **44** 766 (2006); *Teplofiz. Vys. Temp.* **44** 770 (2006)
209. Lundström U, MetalJet X-Ray Sources for High Intensity X-Ray Beams. NIS Colloquium, X-Ray Induced Modifications in Materials: Applications and Challenges (Torino: Univ. di Torino, 2017); http://www.solid.unito.it/XIMM/EXCILLUM.pdf
210. Wiesmann J et al. *Part. Part. Syst. Charact.* **26** 112 (2009)
211. Rackwitz V *J. Anal. Atom. Spectrom.* **26** 499 (2011)
212. Rackwitz V, Warrikhoff A, Hodoroab V-D *J. Anal. Atom. Spectrom.* **29** 458 (2014)
213. Hemberg O E, Otendal M, Hertz H M *Opt. Eng.* **43** 1682 (2004)
214. Larsson D et al. *Rev. Sci. Instrum.* **82** 123701 (2011)
215. Espes E et al. *Proc. SPIE* **9212** 92120J (2014)
216. Graf J et al. *Acta Cryst. A* **73** C1249 (2017)
217. Arndt U W, Gilmore D J *J. Appl. Cryst.* **12** 1 (1979)
218. Aslanov L A *Instrumental'nye Metody Rentgenostrukturnogo Analiza* (Instrumentation Methods for X-ray Structural Analysis) (Moscow: Izd. MGU, 1983)
219. He B B *Two-Dimensional X-Ray Diffraction* 2nd ed. (Hoboken, NJ: Wiley, 2018)
220. Namatane Y et al. *Rigaku J.* **34** (1) 9 (2018)
221. Hinrichsen B, Dinnebier R E, Jansen M, in *Powder Diffraction: Theory and Practice* (Eds R E Dinnebier, S J L Billinge) (Cambridge: Royal Society of Chemistry, 2008) Ch. 14
222. Ponchut C *J. Synchrotron Rad.* **13** 195 (2006)
223. Madden T et al. *J. Phys. Conf. Ser.* **493** 012016 (2014)
224. Ohbuchi A *Rigaku J.* **31** (1) 4 (2015)
225. Basolo S et al. *J. Synchrotron Rad.* **14** 151 (2007)
226. Chupas P J et al. *J. Appl. Cryst.* **36** 1342 (2003)
227. Billinge S J L *Z. Kristallogr. Suppl.* **26** 17 (2007)
228. Toby B H et al. *J. Appl. Cryst.* **46** 1058 (2013)
229. Gelisio L, Scardi P *Acta Cryst. A* **72** 608 (2016)
230. Gruner S M, Tate M W, Eikenberry E F *Rev. Sci. Instrum.* **73** 2815 (2002)
231. Klein C, marXperts GmbH, Application Note (2014)
232. Amemiya Y et al. *Nucl. Instrum. Meth. Phys. Res. A* **266** 645 (1988)
233. Dauter Z, Wilson K S *Acta Phys. Polon. A* **86** 477 (1994)
234. He T et al. *Proc. SPIE* **8142** 81421Q (2011)
235. Product Sheet SC-XRD 31, Order No. DOC-S86-EXS031 V2. Bruker AXS Inc. (2011)
236. Brönnimann C, Trüb P, in *Synchrotron Light Sources and Free-Electron Lasers* (Eds E Jaeschke, S Khan, J R Schneider) (New York: Springer, 2016) p. 995
237. Schmitt B et al. *Nucl. Instrum. Meth. Phys. Res. A* **518** 436 (2004)
238. Hülsen G et al. *AIP Conf. Proc.* **705** 1009 (2004)
239. Philips Analytical X'Celerator *J. Appl. Cryst.* **34** 538 (2001)
240. Dauter Z *Acta Cryst. D* **55** 1703 (1999)
241. Pflugrath J W *Acta Cryst. D* **55** 1718 (1999)
242. Mueller M, Wang M, Schulze-Briese C *Acta Cryst. D* **68** 42 (2012)
243. STOE X-area software manual. STOE and Cie GmbH. September 21 (2011)
244. Wenger E et al. *Acta Cryst. B* **70** 783 (2014)
245. Webb J E, Patent US 3415992 A. Published 10.12.1968, Filed 28.12.1965
246. Pennicard D et al. *MRS Bull.* **42** 445 (2017)
247. Lowe B G, Sareen R A *Semiconductor X-Ray Detectors* (Boca Raton, Fl.: CRC Press, 2014)
248. Awadalla S, Iniewski K (Eds) *Solid-State Radiation Detectors: Technology and Applications* (Boca Baton, Fl.: CRC Press, 2015)
249. Boudet N et al. *Nucl. Instrum. Meth. Phys. Res. A* **510** 41 (2003)
250. Dinapoli R et al. *Nucl. Instrum. Meth. Phys. Res. A* **650** 79 (2011)
251. Hamstra R H, Wendland P *Appl. Opt.* **11** 1539 (1972)
252. Jach T *Nucl. Instrum. Meth. Phys. Res. A* **299** 76 (1990)
253. Kirkland J P et al. *Nucl. Instrum. Meth. Phys. Res. A* **266** 602 (1988)
254. Broennimann Ch et al. *J. Synchrotron Rad.* **13** 120 (2006)
255. Henrich B et al. *Nucl. Instrum. Meth. Phys. Res. A* **607** 247 (2009)
256. Donath T et al. *J. Phys. Conf. Ser.* **425** 062001 (2013)
257. Hatsui T, Graafsma H *IUCrJ* **2** 371 (2015)
258. Ramírez-Jiménez F J *AIP Conf. Proc.* **857** 121 (2006)
259. Kriegner D et al. *J. Appl. Cryst.* **48** 613 (2015)
260. Gerndt E et al. *Nucl. Instrum. Meth. Phys. Res. A* **624** 350 (2010)
261. Gao M et al. *J. Appl. Cryst.* **49** 1182 (2016)
262. "XtaLAB P200" *Rigaku J.* **29** (2) 26 (2013)
263. Shiramata Y *Rigaku J.* **32** (1) 3 (2016)
264. "High-resolution/high-speed 2D photon counting X-ray detector HyPix-300" *Rigaku J.* **30** (2) 38 (2014)
265. Michaelsen C et al. *Adv. X-Ray Anal.* **42** 308 (2000)
266. Hasse B et al. *Proc. SPIE* **10387** 103870B (2017)